Title

ER Aggregation Causes Synaptic Protein Imbalance in Retinitis Pigmentosa Mutant Photoreceptor Neurons

Abbreviated Title

Analysis of ER Aggregation in Photoreceptor Synapses

Authors

Samantha Thompson, Sophie M. Crowder, Maryam Hekmatara, Emily R. Sechrest, Wen-Tao Deng, Michael A. Robichaux

Author Affiliations

Department of Ophthalmology & Visual Sciences and Department of Biochemistry & Molecular Medicine, West Virginia University, Morgantown, WV 26506, United States.

Corresponding Author

Michael A. Robichaux, michael.robichaux@hsc.wvu.edu

Number of pages: 52, **Number of figures:** 8 main, 6 extended, **Abstract word count:** 249**,** **Introduction word count:** 650**, Discussion word count:** 1,496.

Acknowledgements

The work was supported by the National Institute of Health P20-GM144230 (MAR), R01 EY030056 (WD); Knights Templar Eye Foundation (MAR); and WVU startup funds (MR and WD). The authors thank Dr. Abigail Moye and Dr. Melina Agosto for feedback during manuscript preparation. SIM Imaging experiments were performed in the West Virginia University

Microscope Imaging Facility which has been supported by NIH grants P20GM121322 and P20GM144230, the WVU Cancer Institute and the WVU HSC Office of Research and Graduate Education. The Nikon A1R-SIM is supported with funding from U54GM104942 and P20GM103434. The authors declare no competing financial interests.

Abstract

Rod photoreceptor neurons in the retina detect scotopic light by packaging large quantities of the visual pigment protein rhodopsin (Rho) into stacked membrane discs within their outer segments (OS). Efficient Rho trafficking to the OS through the inner rod compartments is critical for long-term rod health since diseases like retinitis pigmentosa (RP) induce Rho mislocalization in these inner compartments, including in the rod presynaptic terminals (i.e., “spherules”). Given the importance of protein trafficking to the OS, less is known about the trafficking of rod synaptic proteins that maintain critical synapses between rods and inner retina neurons. Furthermore, the subcellular impact of Rho mislocalization on rod spherules has not been investigated. In this study we used super-resolution and electron microscopies, along with proteomic measurements of rod synaptic proteins, to perform an intensive subcellular analysis of Rho synaptic mislocalization in P23H-Rho-RFP RP mutant mice of both sexes. We discovered mutant P23H-Rho-RFP protein mislocalized in distinct ER aggregations within the spherule cytoplasm which we confirmed in wild type (WT) rods overexpressing P23H-Rho-RFP. Additionally, we found significant protein abundance differences in Dystrophin, BASSOON, ELFN1 and other synaptic proteins in P23H-Rho-RFP mice. By comparison, Rho mislocalized along the spherule plasma membrane in WT rods and in rd10 RP mutant rods, in which there was no synaptic protein disruption. Throughout the study, we also identified a network of ER membranes within WT rod presynaptic spherules. Together, our findings establish a previously uncharacterized ER-based secretory system that mediates normal trafficking and turnover at mouse rod synapses.

Significance Statement

In the retina, protein trafficking to the outer segments in rod photoreceptor neurons is essential for vision; however, less is known about protein trafficking to the synapses that rods form with downstream retinal neurons. Stressors like retinitis pigmentosa (RP) and other inherited retinal diseases cause widespread rhodopsin (Rho) protein mislocalization in rods, including at the presynaptic terminals. This study examines the subcellular impact of Rho mislocalization on this presynaptic region caused by the P23H-Rho RP mutation and in other contexts. Mutant P23H-Rho-RFP fusion endoplasmic reticulum (ER) aggregation disrupted rod-specific synaptic protein levels, and combined with the detection of an endogenous presynaptic ER network in rods, this study supports a disease-relevant ER-based protein trafficking and turnover mechanism at rod synapses.

Introduction

In the retina, rod photoreceptor neurons detect dim light through the photoactivation of the rod-specific G-protein coupled receptor rhodopsin (Rho). Rho and other visual proteins are densely loaded into stacked membrane discs in the rod outer segment (OS) compartment, which is joined to the inner segment (IS) by a narrow connecting cilium (CC). Mammalian rods have compartmentalized cell bodies preceding the presynaptic terminals (spherules), which form synapses with downstream retinal neurons (Townes-Anderson et al., 1988). Proper Rho protein trafficking to the OS is absolutely essential for long-term rod stability and retinal health (Sung et al., 1994; Lem et al., 1999). Since new OS membrane discs are continuously formed in rods, Rho protein, which is synthesized throughout the cell body and IS, must be constantly fluxed unidirectionally into the OS through various coordinated trafficking mechanisms. Any disruption to the unidirectional flow of Rho into the OS causes Rho mislocalization, which is the typical subcellular outcome of blinding rod diseases caused either by a genetic mutation

(Hagstrom et al., 1999; Guo et al., 2022) or retinal detachment (Fariss et al., 1997; Fisher et al., 2005). Despite the central role of OS protein trafficking in rods, a cellular trafficking system in rods is required to supply and maintain their presynaptic spherules; however, little is known about these trafficking mechanisms and how they might be affected by Rho mislocalization.

Rod presynaptic spherules are located in the outer plexiform layer (OPL) of the retina and contain a tetrad of postsynaptic invaginating neurites (Behrens et al., 2016; Torten et al., 2023). Each rod spherule features a single synaptic ribbon, an electron dense structure that organizes synaptic vesicles for glutamate release in the dark (Moser et al., 2020). Most mouse rods have stereotypical R1 spherules that are connected to the cell body through an axon (or "internal fiber", (Carter-Dawson and Lavail, 1979)), while fewer rods have R2 spherules that are contiguous with cell bodies (Fig. 1 A; (Li et al., 2016)). Critically, rod spherules contain essential proteins that are either structural elements of the synaptic ribbon, like BASSOON, or proteins that localize at the synaptic cleft to form stabilizing trans-synaptic protein complexes, including ELFN1, Dystrophin and Dystroglycan (Furukawa et al., 2020). Disruptions to these rod synaptic proteins lead to functional and structural defects in spherules and often cause irreparable synaptic miswiring (Dick et al., 2003; Omori et al., 2012).

Therefore, rods must utilize a secretory system to maintain their presynaptic spherules that operates in concert with constant protein delivery to the OS. In mouse models retinitis pigmentosa (RP) of photoreceptor degeneration, including for the well-characterized misfolding P23H-Rho mutation (Sung et al., 1991; Kaushal and Khorana, 1994; Saliba et al., 2002), Rho is mislocalized not only to the rod IS and cell body but also the OPL (Roof et al., 1994; Hagstrom et al., 1999; Barhoum et al., 2008). In the *P23H-hRho-Tag-RFP-T* mouse, mutant P23H-hRho-RFP protein mislocalized and accumulated throughout the ER in the IS, ONL, but also in the OPL (Robichaux et al., 2022). Rho mislocalization in the OPL has also been demonstrated in RP dog and human retinas (Milam et al., 1998; Fariss et al., 2000; Beltran et al., 2006), as well as after retinal detachment (Fariss et al., 1997; Fisher et al., 2005); however, the impact of Rho

OPL mislocalization on rod spherule structure and synaptic protein trafficking and turnover has never been investigated.

Here, we performed a detailed subcellular analysis of Rho mislocalization in rod spherules. Using *P23H-RFP* mice, we found that P23H-hRho-RFP mutant protein accumulated specifically within the ER of the spherule cytoplasm, as opposed to membrane mislocalization observed in rd10 RP mutant rods or in overloaded WT rods. Mutant P23H-Rho ER aggregations in *P23H-RFP/+* rods interfered with normal rod synaptic protein levels. Combined with evidence of ER membranes in WT rod spherules, our findings establish an ER-based secretory system for presynaptic proteins within mouse rod spherules that is sensitive to protein aggregation.

Materials and Methods

***Animals*.** All WT mice were C57BL/6J. The *P23H-hRho-TagRFPt* (*P23H-RFP*) and the *Rho-GFP-1D4* mice were previously described in (Robichaux et al., 2022; Haggerty et al., 2024) and were also C57BL/6J. The rd10 mice (Jackson Laboratories) were also C57BL/6J and were crossed with *Rho-GFP-1D4* homozygotes to generate rd10;Rho^{GFP} mice. *WT-hRho-TagRFP-T* (*WT-RFP*) mice were generated using CRISPR gene editing in the Genetically Engineered Murine Model Core Facility which is supported by the University of Virginia School of Medicine, Research Resource Identifiers (RRID):SCR_025473. The sgRNA (AGTACTGTGGGTACTCGAAGTGG) and HDR donor oligos (GCCACAGCCATGAATGGCACAGAAGGCCCTAACTTCTACGTGCCCTTCTCCAATGCGACG GGTGTGGTACGCAGTCCCTTCGAGTACCCACAGTACTACCTGGCTGAGCCATGGCAGTTC TCCATGCTGGCCGCCTACATGTTTCTGCTGAT) were developed for correcting the H23 mutant codon (CAC) to the WT P23 (CCC) codon in *P23H-RFP* mice. CRISPR reagents were injected into fertilized zygotes from *P23H-RFP* homozygous male and female mice for germline genome integration. Founder mice were then crossed to C57Bl/6J WT mice. F1 progeny were

screened to confirm that the P23H mutation was corrected by sequencing genomic DNA. There was an unexpected silent change in the genome for residue S22 (AGC to TCA), but this did not change the coded amino acid sequence of hRho. We also validated the *WT-RFP* knockin with western blotting and fluorescence microscopy (Fig. 1 B-C, Fig. 1-1 A-B), and because validation was completed in the middle of this study, we continued using WT mice as controls for comparison to *P23H-RFP* mice throughout these experiments.

All mice were housed in 12 h light/dark conditions. Both sexes were used for experiments in the study unless otherwise noted. Mouse ages for imaging are denoted in the data. All experimental procedures using mice were approved by the Institutional Animal Care and Use Committee of West Virginia University (approval #2102040326).

***Antibodies and Labeling Reagents*.** The following primary antibodies were used in this study: anti-1D4 (Millipore Sigma, Cat# MAB5356); anti-4D2 (Millipore Sigma, Cat# MABN15); anti-Dystrophin (immunofluorescence) (Abcam, Cat# ab15277); anti-Dystrophin (western blotting) (Proteintech, Cat# 12715); anti-Dystroglycan (Proteintech, Cat# 66735); anti-RIBEYE (Synaptic Systems, Cat# 192103); anti-BASSOON (Enzo, Cat# SAP7F407); anti-TUBB5 (Millipore Sigma, Cat# T7816); anti-Sec61β (Cell Signaling Technology, Cat# D5Q1W); anti-Centrin, 20H5 (Millipore Sigma, Cat# 04-1624); anti-ATPB2 (Proteintech, Cat# 22338); FluoTag-X2 anti-PSD95-Alexa647 nanobody (NanoTag Biotechnologies, Cat# N3702-AF647). The anti-ELFN1 polyclonal antibody was a gift provided by Dr. Kirill Martemyanov (University of Florida Scripps Institute). The anti-mGluR6 polyclonal antibody was a gift provided by Dr. Melina Agosto (Dalhousie University) (Agosto et al., 2021).

The following secondary antibodies were used in this study: F(ab')2-goat anti-rabbit Alexa 488 IgG (Invitrogen, Cat# A11070); F(ab')2-goat anti-mouse Alexa 488 IgG (Invitrogen, Cat# A11017); F(ab')2-goat anti-rabbit Alexa 647 IgG (Invitrogen, Cat# A21246); F(ab')2-goat anti-mouse Alexa 647 IgG (Invitrogen, Cat# A21237); F(ab')2-goat anti-mouse Alexa 555 IgG

(Invitrogen, Cat# A21425); IRDye800CW goat anti-rabbit IgG (LI-COR, Cat# 925-32211); IRDye800CW goat anti-mouse IgG (LI-COR, Cat# 925-32210). Wheat germ agglutinin (WGA) staining was performed with WGA-CF640R (Biotium, Cat# 29206) and WGA-Alexa-CF488A (Biotium, Cat# 29022).

Retinal Immunofluorescence. For immunofluorescence staining of mouse retinal cryosections for confocal microscopy, mouse eyes were enucleated, and the cornea, lens, and optic nerve were removed in ice cold 4% (wt/vol) paraformaldehyde (PFA) fixative. Eyecups were fixed for an additional 15 min at room temperature and transferred to a 30% sucrose in 1x phosphate-buffered saline (1xPBS) solution for 2 h on ice. Eyecups were further cryopreserved in a 1:1 mixture (OCT:30% sucrose) overnight at 4°C. Cryopreserved eyecups were frozen in optimal cutting temperature medium (OCT). 5 µm cryosections were cut on a Medical Equipment Source 1000+ cryostat, mounted onto Superfrost Plus slides (VWR Cat# 48311-701), and stored for less than 48 hours at -80°C. For immunostaining, slides were warmed to room temperature prior to antigen retrieval in a 1X antigen retrieval solution (VWR, Cat# 103780-314) for 5 min at 80°C. Slides were equilibrated to room temperature, rinsed with 1xPBS, and incubated in an antibody blocking solution (10% Normal goat serum (NGS) + 0.1% Triton X-100 in 1xPBS) for 1 h at room temperature. Sections were incubated in 1–2 µg of primary antibodies diluted another blocking solution (2% NGS + 0.1% Triton X-100 in 1xPBS) at room temperature for 1 h. Sections were washed with PBS-T (0.1% Tween-20 in 1xPBS) 4 times for 5 min each prior to incubation with secondary antibodies diluted 1:500 in the same antibody blocking solution for at room temperature 1 h. Sections were washed in PBS-T and counterstained with 0.2 µg/ml 4′,6-diamidino-2-phenylindole (DAPI) (Thermo Fisher Cat# 62248) diluted in 1xPBS at room temperature for 20 min. Sections mounted with ProLong Glass Antifade Mountant (Thermo Fisher Scientific Cat# P36980).

For immunofluorescence labeling of whole retinas for structure illumination microscopy (SIM), mouse eyes were enucleated, and corneas were punctured and fixed in a 4% PFA + Ames' media (Sigma Cat# A1420) fix solution for 15 min at room temperature. After the initial fixation, retinas were removed, bisected, and cut into trapezoid segments. Retinal segments were fixed in 4% PFA + Ames' media for an additional 45 min at room temperature for a total 1 h fixation. Retinas used for anti-Sec61β ER immunolabeling were lightly fixed for only 5 min total and stained as whole retinas. Retinas were quenched in 100 mM glycine in 1X PBS for 30 min at 4°C and then incubated in SUPER block buffer (15% NGS, 5% bovine serum albumin (BSA) (Sigma, Cat# B6917) + 0.5% BSA-c (Aurion, VWR, Cat# 25557) + 2% fish skin gelatin (Sigma, Cat# G7041) + 0.05% saponin (Thermo Fisher, Cat# A1882022) + 1× protease inhibitor cocktail (GenDepot, Cat# P3100-005), in half dram vials (Electron Microscopy Sciences, Cat# 72630–05) for 3 h at 4°C. Retinas were incubated with 5 µg of primary antibodies that were spiked into the block buffer for 3 full days, at 4°C with gentle agitation. A second dose of either Rho or Sec61β antibodies was added on the second day of primary antibody incubation to improve labeling. Retinas were washed 6 times with 2% NGS in Ames' for 10 min each on ice prior to incubate with 4 µg of secondary antibodies in 2% NGS in Ames + 1X protease inhibitor cocktail for 12-16 h (overnight) at 4°C. Retinas were washed 6 times with 2% NGS in Ames' 5 min each on ice and post-fixed in 2% PFA in 1xPBS for 30 min at room temperature with gentle agitation. Post-fixed retinas were then dehydrated with the following steps of pure ethanol diluted in water: 50%, 70%, 90%, 100%, 100%. Each ethanol step was performed at room temperature for 15 min with mild agitation. Following dehydration, retinas were embedded in Ultra Bed Low Viscosity Epoxy resin (Electron Microscopy Sciences, EMS Cat# 14310) using the following steps (all room temperature with gentle agitation): 1:3 resin to 100% ethanol for 2 h; 1:1 resin to 100% ethanol for 2 h; 3:1 resin to 100% for approximately 16 h (or overnight); 2 steps of full resin (no ethanol) 2 h each. Embedded retinas were then mounted in molds and cured for 24 h at 65°C. Resin blocks were trimmed and sectioned using glass knives on a Leica UCT

Ultramicrotome to obtain 1 to 2 µm sections which were mounted on #1.5 glass coverslips with ProLong Glass mountant.

RNAScope. Frozen 5 µm retinal sections were collected on Superfrost Plus slides as described above. Sections were dried for 1 h at -20°C and stored overnight at -80°C. The RNAScope Multiplex Fluorescent Reagent Kit v2 (Advanced Cell Diagnostics, ACD, Cat# 323110) was used for RNA detection, as follows. Sections were postfixed with 4% PFA in 1xPBS for 5 min at room temperature and then dehydrated in ethanol steps (50%, 70%, 100%, 100%) for 5 min each step. Sections were dried and treated with hydrogen peroxide for 10 min at room temperature. Sections were then incubated in boiling Co-Detection Target Retrieval (ACD, Ref#322000) for 2 min and then rinsed in water before incubation with 1 µg anti-centrin primary antibody (Millipore Sigma, Cat# 04-1624) overnight at 4°C. The following day, sections were fixed in a 10% neutral buffered formalin solution for 30 min at room temperature, washed, and incubated with Protease III (ACD, Cat# 322381) for 30 min in a 40°C hybridization oven. The RNA probes for *POLR2A*/positive control (ACD, Ref# 320881), *dapB*/negative control (ACD, Ref#320871), and *Elfn1*/Mm-Efln1 (ACD, Ref#449661) were added onto sections for a 2 h incubation at 40°C. Amplification steps were then subsequently performed per manufacturer instructions. Sections were then incubated with the HRP-C1 reagent (ACD, Cat# 323110) followed by the TSA vivid dye (ACD Cat# 323271, 1:25,000 diluted in TSA buffer (ACD, Ref# 322809)) for 30 min at 40°C for probe visualization. Finally, sections were incubated with secondary antibody (F(ab')2-goat anti-mouse Alexa 647, diluted 1:500) for 1 h at room temperature. Sections were counterstained with DAPI for 30 seconds and mounted with ProLong Glass Antifade Mountant. Slides were imaged on a Nikon N-SIM E microscope system (see below), and z-projections (step size = 0.2 µm) were obtained for reconstruction. RNA probe SIM channels (488 nm) were processed for additional 3D deconvolution. Identical acquisition settings were used for each imaging field.

Fluorescence Microscopy. Confocal microscopy was performed on either a Nikon C2 inverted confocal microscope, a Nikon AX inverted confocal microscope or a Nikon CrestV3 spinning disk microscope. Quantitative confocal imaging was performed either on the C2 and AX systems using Plan fluor 40x/1.30 NA (C2), Plan flour 40x/1.30 DIC H N2 (AX), or Plan Apo λ 100x/1.45 NA oil immersion objectives. 405 nm, 488 nm, 561 nm, and 640 nm laser lines were used on both systems. The CrestV3 spinning disk system was equipped with a Hamamatsu Fusion Gen III sCMOS camera, and a Plan Apo λD 60×/1.42 NA oil objective was used with Lumencor Celesta 405 nm, 477 nm, 546 nm, and 638 nm laser excitation. For all confocal imaging, identical acquisition settings were used between age-matched WT control and mutant sections, which were always mounted and immunolabeled on the same slide. Confocal images were acquired using Nikon NIS-Elements software and processed and analyzed using Fiji/ImageJ (Schindelin et al., 2009). SIM imaging was performed at room temperature as described in (Haggerty et al., 2024) using a Nikon N-SIM E microscope system equipped with a Hamamatsu Orca-Flash 4.0 camera and a SR HP Apochromat TIRF 100X, NA 1.49 oil immersion objective. Z-projections were obtained with 0.2 µm Z-steps (5-10 steps per image). SIM images were reconstructed using the NIS-Elements software and in some cases were additionally processed in NIS-Elements for 3D deconvolution using Automatic deconvolution mode. SIM images were processed and analyzed using Fiji/ImageJ.

AAV Subretinal Injections. AAV constructs were designed and purchase from VectorBuilder. All AAV constructs contain a mouse rod specific MOPS500 promoter (Flannery et al., 1997). Human *RHO* coding sequences were tagged with an in-frame C-terminal TagRFP-T or EGFP. All AAVs contained an internal ribosome entry site (IRES) with a complimentary fluorescent tag (EGFP or mCherry) for visualization of AAV infection. AAVs were produced and packaged in the WVU Biochemistry and Molecular Medicine Virology Core. 3 adult WT mice were injected with each AAV. Subretinal injections were performed as in (Sechrest et al., 2024): prior to subretinal

injection, mouse eyes were dilated with Tropi-Phen drops (Pine Pharmaceuticals). Mice were anesthetized using ketamine (80 mg/kg) and xylazine (10 mg/kg) in sterile 1xPBS via intramuscular injection. Fluorescein dye was added (0.1% final concentration) to AAVs for visualization. A 25-gauge needle was used to puncture the edge of the cornea. Transcorneal subretinal injections were performed by inserting a 33-gauge blunt end needle attached to a 5 µL Hamilton syringe containing 1 µL of AAV and injecting into the subretinal space. After injection, a Neomycin + Polymixin B Sulfates + Bacitracin Zinc ophthalmic ointment (Bausch & Lomb) was added to the eyes and antisedan (Orion Corporation) was intraperitoneally injected to reverse anesthesia.

21 days post-injection, mice were euthanized, and the injected eyes were enucleated. The corneas were punctured immersed in 4% PFA in Ames' media. Eyes were fixed for 15 min before the cornea, lens, and optic nerve were removed. Eyecups were then embedded in 4% low melt agarose (Lonza, Cat# 50080). 150 µm vibratome sections were collected on a PELCO EasiSlicer vibratome and screened for AAV infection. Sections were stained for SIM by first quenching in a 100 mM glycine solution and blocking with 10% normal goat serum + 0.1% Triton X-100 in 1xPBS. 1-2 µg primary antibodies were spiked into the blocking solution and sections were probed for 12-16 h at 4°C with mild agitation. Sections were washed before incubation with secondary antibodies (diluted 1:500 in 1xPBS) for 2 h at room temperature. Sections were washed and post-fixed with 1% PFA prior to either sucrose cryopreservation and cryosectioning or ethanol dehydration and resin embedding as described above.

Histology. For hematoxylin and eosin (H&E) staining and analysis, WT mice at age P30 (N=3) and *WT-RFP/+* mice at ages P30 and P180 (N=3, each age) were euthanized, and the eyes were enucleated and immediately incubated into Excalibur's alcoholic Z-fix (Excalibur Pathology). Fixed eyes were sent to Excalibur Pathology, Inc. (Norman, OK) for paraffin sectioning and H&E staining. The H&E sections were imaged on a brightfield MIF Olympus

Slide Scanner. 3 H&E retinal sections through the optic disk were used for each of the mice included in the analysis. Photoreceptor nuclei in the ONL were counted in a blinded analysis from an 80 µm wide central retina region located 500 µm for the optic disk for each section.

TEM. Mouse eyes were enucleated, the anterior segments were removed, and the eyecups were immersion fixed in ice cold fixative (4% PFA + 2.5% glutaraldehyde diluted in 1xPBS, pH 7.4) for 12-16 at 4°C with mild agitation. Retinas were dissected from the fixed eyecups and cut into four trapezoidal pieces. Retinas were rinsed with 100 mM cacodylate buffer (pH 7.4) 3 times and post fixed in 1% OsO4 + 1.5% K4[Fe(CN)6] × 3H2O in 100mM cacodylate buffer for 1 h at 4°C with mild agitation. Retinas were then washed three times in a wash solution (100 mM cacodylate buffer + 50 mM Na-maleate, pH 5.0, in water) on ice, 5 min each step. Then, retinas were incubated in 2% uranyl acetate (UA) in 50 mM Na-maleate for 3 h at 4°C with mild agitation. Retinas were washed with 50 mM Na-maleate 3 times and water 3 times on ice for 5 min each step before dehydration with increasing concentrations of ethanol (50%, 70%, 90%, 100%, 100%) and 2 100% acetone steps at room temperature for 15 min each step. Dehydrated retinas were resin-embedded in increasing concentrations of Eponate 12 resin (Ted Pella Inc., Cat#18010) in room temperature/mild agitation stages, as follows: 1:1 resin to acetone overnight; 3:1 resin to acetone 2 h; 2 full resin steps (no acetone), 2 h each. Embedded retinas were transferred to molds and cured at 65°C for 48 hours. Ultrathin resin sections (70 nm) were cute on a Leica UCT ultramicrotome using a Diatome Ultra 45° diamond knife and collected on copper grids (Electron Microscopy Sciences, Cat# G100-Cu). Copper grids were post stained with a 1.2% UA solution and a 3% lead citrate solution (Electron Microscopy Sciences Cat#22410) for 4 min each. Grids were imaged on either a Joel JEM 1010 transmission electron microscope or a Joel 1400 transmission electron microscope.

TMT-MS. Whole mouse retinas were dissected for tandem mass tag mass spectrometry (TMT-MS) in sterile 1xPBS, and the ciliary bodies were removed. Retinas from both eyes of each mouse were combined and flash-frozen on dry ice. For P30 analysis, 3 WT and 3 *P23H-RFP/+* males were used. For P90 analysis, 3 WT female and 4 *P23H-RFP/+* female mice were used. Frozen retinal samples were sent to IDEA National Resource for Quantitative Proteomics (Little Rock, AR) for lysis, trypsin digestion, TMT labeling and Orbitrap Eclipse MS acquisition. Database analysis, quality control, normalization, fold change calculations and statistical testing (described below) were performed by IDEA.

Western Blotting. 3 WT and 3 *P23H-RFP/+* mice were used for age P30 and P90 western blot analyses. Dissected retinas were flash frozen on dry ice for at least 10 min, resuspended in 100 µl of 1% Triton X-100 + 1X protease inhibitor (Thermo Fisher, Cat#A32955) in 1xPBS and lysed by sonication. Lysed samples were cleared with centrifugation, and 11 µl of each sample was combined with 11 µl of urea sample buffer (6 M urea + 140 mM SDS + 0.03% bromophenol blue + 360 mM BME in 0.125 M Tris (pH 6.8)) and heated for 5 min at 95°C. Samples were loaded into a Novex Tris-glycine mini 4-12% gel (Thermo Fisher Cat# XP04120) for SDS-PAGE. Gels were transferred onto Immobilon-FL Transfer Membrane polyvinylidene difluoride (PVDF) (pore size: 0.45 µm) (LI-COR Cat# 92760001) in Tris-Glycine Transfer Buffer (Bio-Rad Cat# 1610771). Blots were blocked with Intercept Blocking Buffer (LI-COR, Cat# 927–6000) for 1 h and then washed 3 times with PBS-T 5 min each. Primary antibodies at 1:500 to 1:20,000 dilutions in PBS-T were added to the blots for 2 h probing at room temperature. Blots were washed and secondary antibodies (diluted 1:50,000 in PBS-T) were added for 1 h probing at room temperature. Blots were imaged on an Amersham Typhoon scanner (GE).

Deglycosylation Assay. Deglycosylation assays were performed as in Haggerty et al. (2024): dissected retinas were flash frozen at -80°C for 10 minutes and then lysed in 100 µL of RIPA

buffer (Alfa Aesar, Cat# J63306) + protease inhibitor cocktail (GenDepot Cat# P3100-001). Samples were cleared with centrifugation and the cleared supernatant was used for the assay. Lysate was mixed with deglycosylation buffer containing PNGase F (New England Biolabs, Cat# P6044) and incubated for 10 min at 37°C. Protein deglycosylation mix II (New England Biolabs, Cat# P6044S) was added to the treated tubes and buffer only was added to the control tubes. All samples were then incubated for 1 h at 37°C. Samples were cooled on ice for up to 10 mins and mixed with urea sample buffer for a 1:1 mixture and loaded onto IVGN Novex WW 10-20% Tris-Glycine gels (Fisher Scientific, Cat# 89238-778) for western blotting, as described above.

Image Processing and Analysis. For confocal image puncta analyses (Fig. 5 E-F, Fig. 5-1 C-D; Fig. 7 J), channels of interest were cropped a width of 80 µm and coded for a blinded analysis. For Dystrophin and BASSOON, integrated densities of 10 individual puncta were measured for each of 4 images per mouse included in the analysis (40 puncta per mouse total). An equal number of mean background measurements were taken for each image. The average mean background was multiplied by the puncta areas and these values was used for background subtraction. For the ELFN1 OPL particle analysis, the OPL was selected based on DAPI staining and thresholding was used to collect the foreground ELFN1 puncta signal and background for each image. Thresholding values were identical for all images and conditions. For ELFN1 and mGluR6 ONL vs OPL intensity measurements (Fig. 6 A-D, Fig. 6-1 C), mean intensity values were measured from ONL and OPL regions, which were selected based on the DAPI channel. For the RFP puncta analysis, channels were selected as before, and puncta were preselected and coded based on their association (RFP+) or lack of association (RFP-) with RFP signal for blinded integrated density measurements. RNAscope puncta were counted from SIM z-projections by selecting IS, ONL and OPL regions based on the centrin immunostaining and DAPI channels. In SIM images, the distal ONL (dONL) was distinguished in images focused on the IS region from the proximal ONL (pONL) in images focused on the OPL.

Analyze Particles in FIJI/ImageJ was used for puncta counting in each region, and the same thresholding values were used for all images. For TEM, images that contained a clear ribbon in the front-view, rod-like orientation were selected for a blinded analysis based on the parameters described in (Kesharwani et al., 2021). The ribbon height was manually measured from the anchoring site to the ribbon tip, and the synaptic vesicles were manually counted and considered ribbon-associated if they overlapped or had clear tethers to the ribbon. For western blotting, the intensities of the bands from the blot scan images were measured using Fiji/ImageJ. Background measurements were also taken from the same area as the measured bands for background correction.

Experimental Design and Statistical Analysis. Specific experimental design details, such as number of mice and cells examined, are included in the Results text or the figure legends. All confocal analyses were performed with matching retinal sections between experimental and WT control conditions. Experimental datasets were directly compared to the matching WT data, and thus all data were normalized for aggregation so that WT mean values = 1. To statistically compare the aggregated data, standard deviations were propagated to determine the relative error, and the propagated standard deviations are represented as error bars in each of the aggregated data graphs. For TMT-MS data, volcano plots were generated using VolcaNoseR (Goedhart and Luijsterburg, 2020), and gProfiler was used to classify proteins based on the Gene Ontology Cell Compartment/GO-CC terms: “photoreceptor outer segment,” “synapse,” “photoreceptor inner segment,” and “photoreceptor connecting cilium.” TMT-MS data were statistically compared with a differential abundance analysis and moderated t-tests to account for protein variability, distribution, and abundance. For each comparison, P-values and false discovery adjusted P-values were calculated. All graphs were generated using GraphPad Prism and all statistical testing was performed in either GraphPad Prism or GraphPad Quickcalcs.

Results

Mutant P23H-Rho-RFP protein is mislocalized within the cytoplasm of rod presynaptic spherules

To exclude the possibility that Rho mislocalization in *P23H-hRho-TagRFP-T* (hereafter *P23H-RFP*) heterozygous knockin mouse retinas is the outcome of the P23H-Rho misfolding mutation rather than an effect of the C-terminal TagRFP-T fusion tag, a new *WT-hRho-TagRFP-T* mouse line (hereafter "*WT-RFP*" in reference to the knockin mouse) was generated with a restored WT P23 residue in the *hRho-RFP-TagRFP-T* knockin allele. As in the *P23H-RFP* mice, an additional 1D4 sequence is included at the C-terminus of the *WT-RFP* allele. In *WT-RFP/+* heterozygous retinas, WT-hRho-TagRFP-T fusion protein (hereafter WT-hRho-RFP) was localized exclusively in the OS layer (Fig. 1 B-C). By comparison, in *P23H-RFP/+* heterozygous mouse retinas, P23H-hRho-TagRFP-T protein (abbreviated P23H-hRho-RFP) was mislocalized throughout the IS, ONL, and OPL at ages P30 and P90 (Fig. 1 B-C) as described previously (Robichaux et al., 2022). The normal OS localization of WT-hRho-RFP demonstrates that Rho mislocalization in *P23H-RFP/+* rods is triggered by the P23H-Rho mutation, not the TagRFP-T fusion tag. Additionally, western blotting with the 1D4 Rho monoclonal antibody (Molday and MacKenzie, 1983) was used to demonstrate a ~65 kDa band corresponding to the WT-hRho-RFP protein in *WT-RFP/+* retinas (Fig. 1-1 A). A deglycosylation assay also confirmed that WT-hRho-RFP was glycosylated just like endogenous mouse WT Rho protein and WT Rho-GFP-1D4 protein from the *Rho-GFP-1D4/+* mouse (Robichaux et al 2022; Haggerty, 2024) (Fig. 1-1 B). ONL density was quantified to compare P30 WT retinas to P30 *WT-RFP/+* retinas, revealing no significant difference (Fig. 1-1 C), which demonstrates that *WT-RFP/+* rods are stable at this age. However, there was ONL photoreceptor nuclei loss in P180 *WT-RFP/+* retinas indicating late-stage instability. In a separate analysis, ONL nuclei counts in *WT-RFP/+* retinas were significantly higher than those in age-matched *P23H-RFP/+* retinas at both P30 and P90 (Fig. 1-1 D).

Next, SIM super resolution microscopy was used to closely examine the mislocalization of P23H-hRho-RFP mutant protein in the OPL of *P23H-RFP/+* retinas. At P30, *P23H-RFP/+* retinas were shown to be in an early stage of degeneration, before significant photoreceptor loss occurred (Robichaux et al., 2022). In the previous study, we focused on characterizing the mislocalized OPL Rho through co-labeling with ER markers. In the current study, we investigated P23H-Rho-RFP mislocalization within OPL using rod presynaptic spherule markers. *P23H-RFP/+* and age-matched WT retinas were co-immunolabeled with the 1D4 monoclonal Rho antibody, a RIBEYE antibody to visualize synaptic ribbons, and a PSD95 fluorescent nanobody to visualize the presynaptic spherule plasma membranes (Koulen et al., 1998). The samples were then imaged with SIM. In the OPL of P30 WT retinas, PSD95+ rod spherule plasma membranes encased single RIBEYE+ synaptic ribbons that typically appear as horseshoe-shaped structures (Fig. 1 D, Fig. 1-1 E). These rod spherules were distinguishable from cone presynaptic pedicles, which have multiple short ribbons. In P30 *P23H-RFP/+* retinas, bright aggregates of mislocalized Rho protein were located inside some of the rod spherules in the OPL (Fig. 1E, white arrows). Rho aggregations were detected in 28.3% ± 8.6% (mean ± SD, N=3 mice) of all P30 *P23H-RFP/+* rod spherules imaged with SIM. Upon closer observation of individual *P23H-RFP/+* rod spherules, mutant Rho aggregates were localized within the cytoplasm typically near the synaptic ribbons (Fig. 1 F, Fig. 1-1 F-G). In some spherules, there was a partial overlap in 1D4 and RIBEYE signals, and in some cases, the cytoplasmic P23H-hRho-RFP aggregates formed a swirling pattern of bright fluorescence surrounding a dark patch (white asterisks in Fig. 1F and Fig. 1-1 G). RIBEYE+ synaptic ribbons appeared intact in most of the mutant *P23H-RFP/+* spherules examined. We also observed many cases of a small RIBEYE+ puncta in the cytoplasmic space in both WT and *P23H-RFP/+* spherules; in *P23H-RFP/+* spherules, these RIBEYE+ puncta often colocalized with the mutant P23H-hRho-RFP aggregates (Fig. 1-1 F-G). These small RIBEYE+ puncta could represent recycling synaptic ribbons (Adly et al., 1999; Schmitz et al., 2012). While most 1D4+ P23H-hRho-RFP aggregates

were observed as distinct puncta localized near a synaptic ribbon, in some cases, such as in R2 spherules, the 1D4+ P23H-hRho-RFP in the spherule cytoplasm formed a continuous network with the cytoplasm surrounding the adjacent cell body nucleus (Fig. 1 F, magenta arrows).

The same SIM analysis was performed in *P23H-RFP/+* mice at age P90. At this age, *P23H-RFP/+* mice have significant photoreceptor degeneration, but the surviving rods were shown to be adaptive to the mutation, as the rate of degeneration and cell loss reduces after P90 (Robichaux et al., 2022). Here, in P90 mutant *P23H-RFP/+* rods, the mislocalized P23H-hRho-RFP protein accumulated in the OPL in a similar pattern as age P30 mutant rods (Fig. 1 G, Fig. 1-1 H-J). Prominent Rho aggregations were detected in 24.4% ± 5.9% (mean ± SD, N=3 mice) of all P90 P23H-RFP/+ rod spherules imaged with SIM. In individual P90 mutant spherules, large P23H-hRho-RFP aggregations were again localized inside of the spherule cytoplasm, typically close to the ribbons, and were often observed in a swirling pattern around an empty gap in fluorescence. Thus, based on our SIM analysis, large cytoplasmic aggregations of mutant P23H-hRho-RFP protein occur in ~25% of the spherules in the *P23H-RFP/+* rods at P30, and this phenotype persists in the surviving mutant rods at age P90.

AAV overexpression of P23H-Rho and R135L-Rho in WT rods leads to synaptic mislocalization

To test if the P23H-Rho mutation causes mislocalization in the OPL of rod photoreceptors with a non-disease, healthy genetic background, AAVs expressing P23H-hRho-TagRFP-T (P23H-hRho-RFP) or R135L-hRho-EGFP (R135L-hRho-GFP) mutant Rho fusions driven by the rod-specific minimal mouse opsin promoter (Pawlyk et al., 2005) were subretinally injected in adult WT mice. The R135L-Rho mutant was analyzed alongside P23H-Rho because a R135L-Rho-GFP fusion was previously shown to be mislocalized to the OPL when electroporated into WT rat rods (Hsu et al., 2015). While P23H-Rho is a class 2 autosomal dominant RP mutation that misfolds and causes ER retention, R135L-Rho is a class 3 RP

mutation that causes mutant protein accumulation in the endocytic pathway (Chuang et al., 2004; Aguilà et al., 2014; Athanasiou et al., 2018). As controls, WT-hRho-RFP and WT-hRho-GFP AAVs were generated to express WT-Rho fusion proteins in WT rods. All AAV constructs includes a C-terminal 1D4 tag fused in-frame after RFP or GFP.

3 weeks after subretinal AAV injection, retinas were screened with fluorescence microscopy to identify areas of high infection and no injection damage. Compared to WT-hRho-RFP, which predominantly localized correctly to the OS in transduced WT rods, P23H-hRho-RFP was mislocalized as bright puncta in the IS, encircling the nuclei throughout the ONL, and as distinct puncta in the OPL in transduced rods (Fig. 2 A, B). This mislocalization pattern phenocopies the *P23H-RFP/+* mice and demonstrates that the P23H-hRho-RFP mislocalization is caused by the P23H-Rho mutation and not by non-autonomous effects in the disease-model transgenic mouse rods. WT-hRho-GFP also predominantly localized to the OS layer in transduced WT rods, while R135L-hRho-GFP accumulated as bright puncta at the IS/OS junction and mislocalized in a less bright but more consistent, diffuse pattern throughout the IS, ONL and OPL (Fig. 2 C, D). Additionally, while WT Rho fusions were strictly localized in the OS in most WT transduced rods, there were some sporadic transduced rods with clear overexpression of WT-Rho fusion protein that mislocalized to the other photoreceptor cell layers (Fig. 2-1 E-F).

Next, AAV-transduced WT retinas were imaged with SIM to visualize the mislocalization of the mutant P23H-hRho and R135L-hRho fusion proteins in single rod spherules on a subcellular scale. First, cryosections of AAV-transduced retinas were used to preserve the Tag-RFP-T and EGFP fluorescence and were co-immunolabeled for PSD95 to label rod spherule plasma membranes for comparison to the RFP or GFP signal. In these samples, the mislocalized P23H-hRho-RFP in the OPL were bright aggregates, while no consistently strong signal above the background in the OPL was detected in control WT-hRho-RFP transduced retinas (Fig. 2 G). In single spherules, the P23H-hRho-RFP aggregates were localized within

the cytoplasm, which phenocopies the subcellular localization of mislocalized P23H-hRho-RFP aggregates in the OPL of *P23H-RFP*/+ retinas. R135L-hRho-GFP mislocalization was also bright and apparent in the OPL of AAV-transduced WT retinas compared to WT-hRho-GFP, which was not detected in the OPL for most transduced areas (Fig. 2 H). In single spherules, mislocalized R135L-hRho-GFP did not aggregate like P23H-Rho-RFP; instead, it colocalized at the plasma membrane with PSD95 and internally in a pattern that suggests that the mislocalized R135L-hRho-GFP also fills into the spherule plasma membrane surrounding the postsynaptic invaginations (Fig. 2 H, yellow arrows).

For enhanced SIM resolution, we prepared thin plastic sections of AAV-transduced retinas. In this case, the Rho fusions were immunolabeled with the 1D4 antibody along with RIBEYE co-immunolabeling of the rod synaptic ribbons. In these sections, the mislocalized P23H-hRho-RFP aggregates were visualized as swirling patterns of aggregated mutant protein near the synaptic ribbon (Fig. 2 I), again phenocopying the mislocalization pattern described in *P23H-RFP*/+ retinas (Fig. 1 F-G). R135L-hRho-GFP, on the other hand, was localized at the spherule plasma membrane and internally, partially colocalized with the synaptic ribbon (Fig. 2 J), again suggesting that R135L-hRho-GFP fills in the invaginating plasma membrane. Among all WT retinas infected with either WT-hRho fusion, we observed a few examples of 1D4 staining in the OPL in sporadic cells with dramatically overexpressed levels of WT-Rho. In these overloaded rod spherules, WT-hRho-RFP and WT-hRho-GFP were mislocalized along the axons and throughout the spherule plasma membrane, including within the plasma membrane surrounding the synaptic invaginations (Fig. 2 K, L) in a pattern similar to R135L-hRho-GFP mislocalization.

P23H-Rho synaptic mislocalization does not cause ultrastructural defects in rod synaptic ribbons

Based on the observation throughout our SIM analysis that mislocalized P23H-Rho-RFP occupied a significant amount of the rod spherule cytoplasm, we hypothesized that these mislocalized cytoplasmic aggregates disrupted the rod presynaptic machinery on an ultrastructural level. In transmission electron microscopy (TEM) images of P30 WT mouse retinas, rod spherules have a distinct plasma membrane that surrounds the invaginating post-synaptic neurites, an electron dense presynaptic ribbon that extends from the active zone, a cytoplasm filled with synaptic vesicles, and a large mitochondrion (Fig. 3 A). In many spherules, clusters of electron dense endocytic vesicles that are denser than other cytoplasmic synaptic vesicles were observed (Fig. 3 A and Fig 3-1 A, green arrowheads) (Fuchs et al., 2014). Additionally, more irregular membranes were found surrounding the spherule's mitochondrion (Fig. 3 A and Fig 3-1 A, orange arrowheads), in a manner similar to ER membranes previously observed around mitochondria in other neurons (Wu et al., 2017) and in cat cone presynaptic pedicles (Lovas, 1971). Most P30 *P23H-RFP/+* mutant rod spherules had normal TEM ultrastructure, except in cases where electron dense bundles of folded membranes were observed within the spherule cytoplasm (Fig. 3 B-C, orange arrows). The ultrastructure of these stacked membranes matches the semi-organized membrane stacks observed with TEM in the IS layer of *P23H-RFP/+* retinas (Robichaux et al., 2022), and they also match the localization and relative size of the P23H-Rho-RFP puncta observed in Figure 1. Therefore, we conclude that these are expanded stacks of ER membranes within *P23H-RFP/+* spherules that are filled with mislocalized and accumulated P23H-Rho-RFP protein.

In some *P23H-RFP/+* rod spherules, the dense ER membrane stacks were less compact or potentially discontinuous (Fig. 3-1 B); however, in most spherules, some portion of the ER membrane stacks closely localized near the spherule's mitochondrion. In all cases, the long continuous ER membranes were distinct from the electron dense endocytosed vesicles. In one P30 *P23H-RFP/+* R2 spherule, in which the spherule cytoplasm is continuous with the rod cell

body, accumulated stacks of ER appeared to spill over from the cell body cytoplasm into the spherule cytoplasm (Fig. 3 D).

Despite these large ER accumulations, there appeared to be no other major ultrastructural changes to the spherules or the synaptic ribbons in our P30 *P23H-RFP/+* TEM data. To confirm that the ribbon ultrastructure was unaffected, we measured the ribbon height and quantified the number of synaptic vesicles associated with the ribbons in TEM images of P30 WT and *P23H-RFP/+* spherules, and no significant differences were found. The average synaptic ribbon height in WT spherules was 349.4 nm ± 58.1 nm (average ± SD, N=53 ribbons, N=3 mice), while the average *P23H-RFP/+* ribbon height was 348.2 nm ± 85.1 nm (N=68 ribbons, N=3 mice). For WT spherules, the average number of ribbon-associated synaptic vesicles was 7.7 ± 1.8 per ribbon (N=46 ribbons, N=3 mice), while in *P23H-RFP/+* spherules, the average number of ribbon-associated synaptic vesicles was 7.4 SVs ± 2.4 SVs per ribbon (N=65 ribbons, N=3 mice).

The TEM ultrastructure of P90 WT rod spherules was similar to P30; however, there were more noticeable ER-like membranes surrounding the WT spherule mitochondria at this age (Fig. 3 E). Based on our collective observations, we conclude that the irregular membranes surrounding the spherule mitochondria in P30 and P90 rod spherules are part of an endogenous network of ER within the spherule cytoplasm. In one P30 WT spherule TEM image, a portion of the axon was captured in a cross-section with the spherule from the same rod, and irregular membranes were observed within the axon shaft and possibly within a continuous network with the ER surrounding the spherule mitochondrion (Fig. 3-1 C). In another image of a P90 WT R2 spherule, elongated ER-like membranes appeared to extend from the ER surrounding the nucleus into the spherule cytoplasm (Fig. 3-1 D). P90 *P23H-RFP/+* mutant spherules also had expanded ER membranes that appeared tethered to the mitochondria (Fig. 3 F). In higher-magnification TEM images of P30 and P90 *P23H-RFP/+* mutant spherules, the expanded ER

567 membrane folds were traced and compared with mitochondrial membranes, and multiple
568 possible ER-mitochondrion contact sites were found in each example (Fig. 3 G-H).
569
570 ***P23H-Rho-RFP mislocalization causes specific changes in the abundance of rod***
571 ***presynaptic proteins***
572 Since the persistent accumulation of mutant P23H-Rho protein within large ER folds in
573 the cytoplasm of *P23H-RFP/+* rod spherules caused no significant ultrastructural defects to the
574 synaptic ribbons, we considered if the distension of the ER membranes in the spherules and cell
575 bodies of *P23H-RFP/+* rods disrupted normal rod synaptic protein levels. In rod photoreceptor
576 spherules, the ribbon is composed of structural proteins, including RIBEYE (Schmitz et al.,
577 2000) and BASSOON (Bsn, (Dick et al., 2003)), and the ribbon is located just above the
578 synaptic cleft where Cav1.4 L-type voltage-gated calcium channels (made of subunits
579 Cav1.4α1-subunit and Cavβ2-/α2δ4 subunits) are localized and maintained by proteins like the
580 active zone protein RIMS2 (Grabner et al., 2015; Lee et al., 2015). Rods also express cell-
581 adhesion proteins that maintain their trans-synaptic connections with rod ON-type bipolar cells.
582 These include ELFN1, which complexes with postsynaptic mGluR6 (Grm6) (Cao et al., 2015),
583 and Dystrophin (Dmd), Dystroglycan (Dag1), and Pikachurin (Egflam1), which together complex
584 with postsynaptic GPR179 (Sato et al., 2008; Omori et al., 2012; Orlandi et al., 2018; Furukawa
585 et al., 2020) (Fig. 4 A). These trans-synaptic proteins are aligned in the spherule plasma
586 membrane surrounding invaginating ON-type bipolar cell dendrite tips, which was visualized
587 with ELFN1 immunolabeling and SIM (Fig. 4-1 A).
588 To assess protein level differences between *P23H-RFP/+* and WT rods, tandem mass-
589 tag mass spectrometry (TMT-MS) was performed on whole retina samples at ages P30 and
590 P90. At both ages, there were significant peptide abundance changes in *P23H-RFP/+* retinas
591 compared to age-matched WT controls (Fig. 4 B, D). As expected, Rho peptides were
592 significantly downregulated in *P23H-RFP/+* mice at both ages along with peptides for the OS-

specific protein Prph2 and Tulp1, a trafficking regulator in rods localized in the IS, CC, and spherules (Hagstrom et al., 1999, 2001) (Fig. 4 B-E). Peptide abundance for phosducin (Pdc), another OS protein, remain unchanged at P30 (Fig. 4 B-C), but was significantly increased in P90 *P23H-RFP/+* retinas compared to age-matched WT controls (Fig. 4 D-E). Additionally, in P90 *P23H-RFP/+* retinas, peptides for Reep6, an ER protein that was previously localized in the IS and OPL of mice (Agrawal et al., 2017), were significantly increased, while peptides for the rod synaptic proteins Elfn1, Rims2, as well as for Grm6 were significantly decreased (Fig. 4 E). Interestingly, peptide abundance for the rod trans-synaptic receptor Dag1 was significantly increased at P90 in *P23H-RFP/+* rods; however, there were no significant changes for its binding partner, Dystrophin (Dmd), at either age (Fig. 4 D-E). TMT-MS peptide abundance differences for rod synaptic proteins such as Dystrophin may not have been detected due to their expression in other synapses of the inner retina (Wersinger et al., 2011). Dystrophin protein isoforms (the Dp427, Dp260, and Dp140) and Dag1 protein levels were also not significantly changed in western blots from *P23H-RFP/+* and age-matched WT retinas (Fig. 4-1 C).

Next, quantitative confocal microscopy was used to evaluate rod synaptic protein level changes specifically in the OPL of *P23H-RFP/+* and age-matched WT retinas. In confocal fluorescent images, immunolabeled Dystrophin and ELFN1 localized as bright puncta in the OPL among the mislocalized P23H-Rho-RFP, while BASSOON (Bsn) immunolabeled the horseshoe-shaped synaptic ribbons (Fig. 5 A-D). Dystrophin and Bsn were also localized in cone pedicle synapses (Fig. 5 A, arrowheads), which are located proximally to rod spherules in the OPL (Moser et al., 2020). ELFN1 is specific to adult rod spherules (Cao et al., 2015, 2020), although we consistently observed an above-background ELFN1 immunofluorescence signal in the ONL of *P23H-RFP/+* retinas at P30 and P90 (Fig. 5 C-D, Fig. 5-1 A-B).

For Dystrophin and Bsn, a single spherule puncta intensity analysis was performed using confocal imaging to evaluate protein level differences in *P23H-RFP/+* vs. WT rods at ages P30 and P90. At P30 there were no significant differences, but at P90, Dystrophin and Bsn

levels were significantly increased in *P23H-RFP/+* retinas (Fig 5 E, F). Dystrophin and Bsn protein levels were also evaluated along a time course from ages P14 - P365, and P90 was the only time point in which there is a significant difference among these proteins; however, there were consistently higher Bsn levels at older timepoints (Fig. 5 G, Fig. 5-1 C-D). DAPI+ nuclei were counted in all P14-P365 replicate mice in this analysis and plotted in Fig. 5 H, and the rate of photoreceptor degeneration in *P23H-RFP/+* mice closely matches previous measurements (Robichaux et al., 2022). Interestingly, the P90 intensity increases for Dystrophin and Bsn correspond to the approximate timepoint where photoreceptor loss in *P23H-RFP/+* retinas plateaus. ELFN1 is rod-specific in the OPL; therefore, ELFN1 OPL immunofluorescence intensities were compared between *P23H-RFP/+* retinas and age-matched WT mice. At P30, ELFN1 levels in the OPL were significantly reduced in *P23H-RFP/+* retinas but there was no difference at P90 (Fig. 5 I).

Since the RFP+ signal in the *P23H-RFP/+* OPL confocal images were bright, easily detectable puncta, an additional analysis was performed comparing the intensities of Dystrophin and Bsn single spherule signals that were either colocalized with RFP puncta (RFP+) or not (RFP-) in the OPL of P30 and P90 of *P23H-RFP/+* retinas (Fig. 5 J). Although there were no significant RFP+ vs. RFP- differences in the aggregated data (Fig 5-1 E), in some of our P90 *P23H-RFP/+* replicates, Dystrophin and Bsn levels were significantly higher in RFP+ puncta (Fig. 5J), suggesting that spherules with large P23H-Rho-RFP ER aggregates may have higher Dystrophin and Bsn intensity levels than spherules without large aggregations of mutant Rho protein.

We next evaluated the above-background ELFN1 immunofluorescence in the ONL that was observed in *P23H-RFP/+* retinas (Fig. 5 C-D, Fig. 5-1 A-B) by quantifying ELFN1 and mGluR6 localization throughout the outer retina. In P30 *P23H-RFP/+* and age-matched WT retinas, ELFN1 and mGluR6 immunofluorescence were predominantly localized as overlapping puncta in the OPL, and ELFN1 signal was detected in the ONL of both genotypes (Fig. 6 A, B

and Fig. 6-1 A, B). Upon closer analysis of the OPL in these co-labeled sections, there was a significant decrease in ELFN1 and mGluR6 spherule puncta labeling in *P23H-RFP/+* OPLs (Fig. 6 C) but no evidence of mGluR6 mislocalization, which was previously shown in *Elfn1* knockout mice (Cao et al., 2015). Layer-specific pixel intensity measurements from these confocal images confirmed significant reductions in both ELFN1 and mGluR6 in the *P23H-RFP/+* OPL compared to WT controls (Fig. 6 D, Fig. 6-1 C). Interestingly, ELFN1 in ONL was not significantly different between *P23H-RFP/+* vs WT retinas; however, there was a significant increase in the ONL/OPL ratio of ELFN1 in *P23H-RFP/+* retinas (Fig. 6 D), indicating an overall imbalance in the distribution of ELFN1 in *P23H-RFP/+* mutant rods.

Given this imbalance, *Elfn1* mRNA localization and abundance were evaluated using RNAScope fluorescence mRNA detection combined with SIM. With this method, *Elfn1* mRNAs were visualized as bright puncta localized throughout the IS and the ONL photoreceptor subcompartments in both P30 WT and P30 *P23H-RFP/+* retinas (Fig. 6 E), demonstrating that *Elfn1* mRNA distribution was not grossly altered by the protein mislocalization and ER aggregation in *P23H-RFP/+* rods at P30. Notably some *Elfn1* mRNA puncta were localized to the OPL, but these were sporadic and inconsistent. A positive control probe (*POLR2A*) targeting common housekeeping genes and a negative control probe (*dapB*) were analyzed for comparison. RNAScope puncta were counted to quantify any *Elfn1* mRNA abundance changes in the SIM data, and while *Elfn1* mRNA counts were significantly higher in the IS layer and significantly reduced in the OPL in *P23H-RFP/+* vs. WT P30 retinas in aggregated data (Fig. 6-1 C), the counts were variable in the data among the *P23H-RFP/+* replicates (Fig. 6-1 D). *POLR2A* positive control mRNA counts were significantly reduced in the distal ONL (dONL) and OPL in *P23H-RFP/+* retinas, indicating the possibility of a broader, cellular disruption to normal mRNA levels in *P23H-RFP/+* rods (Fig. 6-1 D).

Together, our results suggest that the ER plays a crucial role in rod photoreceptor cell bodies and spherules to ensure the proper delivery and management of rod synaptic proteins.

While previous studies localized the ER throughout the IS, ONL, and OPL in mouse retinas (Krizaj, 2005; Babai et al., 2010; Chen et al., 2015; Agrawal et al., 2017), we validated ER extension into the rod spherule cytoplasm using immunolabeling with Sec61β, an ER marker, and SIM. In both P30 WT and *P23H-RFP/+* retinas, Sec61β ER labeling was distributed throughout all the photoreceptor inner subcompartments (Fig. 6 F-G), but in the *P23H-RFP/+* retinas, larger Sec61β+ puncta were localized to the IS, corresponding the large ER aggregates in those mutant rods. In higher magnification views of the OPL, ER immunofluorescence was clearly localized within the PSD95+ rod spherules in both genotypes (Fig. 6 F-G), demonstrating that the ER network in rod photoreceptors extends from the IS to the rod presynaptic cytoplasm.

Rho mislocalization in rd10 RP mutant retinas does not induce rod presynaptic protein changes

For comparison with our *P23H-RFP/+* model, we next analyzed rd10 mice, an RP model known to exhibit synaptic mislocalization of Rho, in this case non-mutated WT Rho (Barhoum et al., 2008; Zhao et al., 2015). Rd10 mice contain a missense mutation in the beta subunit of phosphodiesterase-6 (PDE6β) that leads to rod degeneration beginning around P18 and peaking at ~P20 (Gargini et al., 2007; Grossman et al., 2009; Jae et al., 2013; Wang et al., 2015; Zhao et al., 2015). Despite this early onset of degeneration, rd10 mutant rod ribbon synapses were shown to be morphologically normal at both P16 and P21 (Grossman et al., 2009). Here, confocal imaging of Rho immunofluorescence was used to examine rd10 retinas, which appeared relatively normal at P16, a pre-degeneration stage (Fig. 7 A), but displayed degenerative morphology by P20 (Fig. 7 B). Based on our imaging, rd10 retinas at P16 and P20 had Rho mislocalization to the IS, ONL, and OPL (Fig. 7 A-B); however, the degree of Rho mislocalization in rd10 P16 retinas was not as robust as expected based on previous reports, nor was the mislocalization as striking as in the *P23H-RFP/+* retinas.

SIM imaging was used to examine the subcellular localization of Rho mislocalization in rd10 mice at P16 and P20. Retinas were immunolabeled with the 4D2 monoclonal Rho antibody (Hicks and Molday, 1986), a PSD95 fluorescent nanobody, and a RIBEYE antibody. While Rho immunofluorescence was detected in the IS and ONL of both P16 WT and rd10 retinas, the amount of Rho throughout the IS and ONL in P16 rd10 rods appeared higher. Rho was also clearly present in the rd10 OPL (Fig. 7 C-E), which together indicates Rho mislocalization at this age. In the IS of P16 WT rods, we detected clear IS plasma membrane labeling (Fig. 7-1 B), while in P16 rd10 rods, mislocalized Rho appeared to aggregate in the Golgi-rich IS myoid region and along the IS plasma membrane (Fig. 7-1 C). In the ONL of both P16 WT and rd10 rods, Rho immunofluorescence surrounded the rod nuclei and also localized to the edges of ~0.5-micron diameter projections corresponding to either the rod axons or the outer fibers that connect mouse rod ISs and cell bodies (Fig. 7-1 D). In P20 rd10 retinas, Rho was also highly mislocalized in the IS compared to age matched WTs; however, OPL mislocalization was not evident at P20 (Fig. 7-1 A) possibly due to advanced degeneration or labeling penetration issues. Notably in control P20 WT retinas, we were unable to detect Rho in the IS and most of the ONL, since P20 WT rods have more developed OSs that limit antibody penetration into the IS and ONL, as we previously described (Haggerty et al., 2024).

In SIM images focused on the OPL in age-matched WT and rd10 mice, Rho immunofluorescence signal was most abundant in P16 rd10 retinas, where mislocalized Rho labeled many teardrop-shaped spherules surrounding the RIBEYE+ rod synaptic ribbons, while in the P20 rd10 OPL, mislocalized Rho immunofluorescence was again less evident (Fig. 7 E). In high magnification images of P16 rd10 rod spherules, mislocalized Rho was predominantly located along the spherule plasma membrane, colocalized with PSD95 (Fig. 7 F, Fig. 7-1 E). In some cases, the mislocalized Rho was also clearly localized along the axon that was continuous with the spherule plasma membrane, while in other cases, Rho appeared to be mislocalized internally, within the spherule cytoplasm and partially colocalized with the

722 RIBEYE+ ribbon (Fig, 7-1 E). However, it was not possible to distinguish if this signal represents
723 Rho within the invaginating spherule plasma membrane, as seen for R135L-hRho-EGFP AAV
724 transduced rods (Fig. 2 H, J) and adult rods overexpressing WT hRho-RFP (Fig. 2 K), or some
725 other internal localization. Importantly, at this magnification, there was no detectable Rho
726 immunofluorescence in P16 WT spherules (Fig. 7-1 F).

727 To confirm this mislocalization pattern, rd10 mice were crossed with the *Rho-GFP-1D4*
728 mice to generate a mouse homozygous for the rd10 mutation and heterozygous for Rho-GFP-
729 1D4 knockin fusion (rd10; $Rho^{GFP/+}$). Using confocal imaging, Rho-GFP was mislocalized in the
730 OPL in P16 rd10; $Rho^{GFP/+}$ retinas compared to control $Rho^{GFP/+}$ retinas (Fig 7 G); however, as
731 with Rho immunofluorescence staining in P16 rd10 retinas (Fig. 7 A-B), the mislocalized Rho-
732 GFP was clearly not accumulated or aggregated in the OPL. With SIM imaging of P16 rd10;
733 $Rho^{GFP/+}$ retinas, Rho-GFP fluorescence was first colocalized with the RIBEYE+ ribbons in the
734 OPL (Fig. 7 H), and then GFP nanobody staining was used to visualize Rho-GFP localization in
735 single rod spherules. The Rho-GFP mislocalization pattern was again predominantly localized
736 along the spherule plasma membrane, encasing the RIBEYE+ synaptic ribbons, with some
737 potentially internal Rho-GFP that could be continuous with the Rho-GFP that was heavily
738 localized in the ONL surrounding the rod nuclei (Fig. 7 I). Additionally, we observed some Rho-
739 GFP signal that branches away from the spherule into the extracellular matrix of the OPL (Fig. 7
740 I, green arrowheads).

741 Finally, rd10 mice at ages P16 and P20 and age-matched WT controls were used to test
742 for any Dystrophin and Bsn protein level changes in the OPL caused by Rho mislocalization.
743 Upon quantitative confocal analysis, no significant differences were found for either protein
744 between WT and rd10 mice at ages P16 and P20 (Fig. 7J), indicating that, unlike in *P23H-*
745 *RFP/+* rods, these synaptic proteins are unaffected by Rho mislocalization in rd10 mice.
746

Discussion

In this study, we found that P23H-Rho-RFP protein accumulated in ER membranes within presynaptic spherules of rod photoreceptor neurons from *P23H-RFP/+* RP mutant mice and that rod presynaptic protein levels were disrupted in these mutants. These results demonstrate the existence of a rod spherule ER secretory system that mediates proper synaptic protein trafficking and turnover and is sensitive to misfolded protein aggregation (Fig. 8). We also found three separate cases in which Rho mislocalized along the spherule plasma membrane: 1) in WT rods expressing non-aggregating but mislocalized RP mutant R135L-hRho-GFP (Fig. 2 H, J), 2) in WT rods overloaded with WT-Rho-GFP/RFP fusion proteins (Fig. 2 K-L), and 3) in rd10 RP mutant rods where a PDE6β mutation disrupts proper Rho trafficking which then overloads the rod plasma membrane (Fig. 7 F, I). Thus, our findings provide new subcellular localization details of how different Rho mislocalization patterns differentially impact mouse rod presynaptic terminals.

While widespread P23H-Rho-RFP protein ER aggregation was clear throughout rods in mutant *P23H-RFP/+* retinas, ER aggregation was not originally apparent in the non-fusion *P23H-Rho/+* knockin mouse model (Sakami et al., 2011). However, a recent study using PROTEOSTAT, a dye that labels aggregated proteins, demonstrated mislocalized Rho aggregation surrounding photoreceptor cell bodies of the ONL in *P23H/+* mouse retinas peaking at age 3 weeks (Vasudevan et al., 2024). They also found that antigen retrieval was needed to detect aggregated Rho in *P23H-Rho/+* with the anti-1D4 Rho antibody, which may explain how P23H-Rho mislocalization was not previously detected with immunolabeling. Nevertheless, in the *P23H-RFP/+* mouse line used in this study, we confirm that ER aggregation of P23H-Rho-RFP extends throughout the rod inner compartments and into the OPL. Additionally, our newly generated *WT-RFP/+* mouse demonstrated that *P23H-RFP/+* mislocalization to synaptic aggregates are specifically triggered by the P23H-Rho mutation (Fig. 1 B-C). Throughout this

772 study, we examined the differences in Rho mislocalization between the *P23H-RFP/+* retinas
773 and other models with SIM, which enabled us to clarify the extent of the ER network in mouse
774 rods.

775 An inter-compartmental rod ER network that reaches the presynaptic spherules was
776 previously described in amphibian rods (Mercurio and Holtzman, 1982). Furthermore, in
777 salamander rods, ER-tracking dye and Ca^{2+} labeling demonstrated a soma-to-terminal ER-
778 based intracellular Ca^{2+} network (Chen et al., 2014, 2015). Mouse rods are morphologically
779 different: the spherules are significantly more segregated from the inner segment than in
780 amphibian rods, such that mouse spherules have their own mitochondria. Additionally, most
781 mouse rod spherules are R1-type, meaning that the spherules are also segregated from the cell
782 body by a thin axon (Li et al., 2016). A study in mice used sarco/endoplasmic reticulum Ca^{2+}-
783 ATPase (SERCA) immunostaining established that presynaptic ER Ca^{2+} release helps sustain
784 prolonged depolarizing conditions in rods (Babai et al., 2010). Our TEM imaging confirms these
785 observations, as we visualized distinct ER-mitochondria associations between the ER and the
786 mitochondrial outer membrane in *P23H-RFP/+* spherules (Fig. 3 G, H). Other TEM studies
787 noted ER membranes wrapped around the mitochondria in WT mouse rod spherules (Ladman,
788 1958; Johnson et al., 2007). Based on this association, the mouse spherule ER may form
789 functional mitochondria-ER contacts that could participate in regulating proper glutamate
790 release, lipid exchange, or Ca^{2+} signaling (Križaj, 2012; Tsuboi and Hirabayashi, 2021) in
791 addition to the role it plays in protein secretion that we propose here.

792 In other neurons, a peripheral ER network has been established as a long-range cellular
793 network for protein trafficking and turnover (Tsuboi and Hirabayashi, 2021). In the axons of
794 various neuronal cell types, a network of smooth ER was shown to form an “anastomosing”
795 network of tubules (Broadwell and Cataldo, 1984; Lindsey and Ellisman, 1985; Konietzny et al.,
796 2023) that wrapped around the mitochondria (Wu et al., 2017; Lee et al., 2018) and had distinct
797 presynaptic ER cisternae branched off from the axonal ER network (Spacek and Harris, 1996;

798 Wu et al., 2017). Based on our TEM imaging, we hypothesize that a similar ER network exists in
799 mouse rod axons that wraps around the spherule mitochondrion and branches off smaller ER
800 cisternae for protein exchange (Fig. 8). Since ER aggregation of P23H-hRho-RFP caused
801 protein abundance changes, this presynaptic rod ER may be integrated with a cellular-wide
802 protein synthesis and trafficking ER network that spans from the distal end of the IS to the
803 spherules. Our finding of visible RFP+ aggregates in only ~1 quarter of rod spherules from P30
804 and P90 *P23H-RFP/+* retinas suggests that the prolific Rho mislocalization throughout the IS of
805 ONL in these mutant retinas (Fig. 1 B, C) likely contributes to the widespread protein changes
806 we measured. The distribution of smooth vs. rough ER in mouse rods remains an open question
807 for future studies; the ER in our TEM data are densely stained and difficult to classify, but since
808 we detected *Elfn1* and *POLR2A* mRNA throughout the IS, ONL and possibly the OPL (Fig. 6 E),
809 it is likely that rough ER is present in each of these compartments.

810 Among the synaptic protein abundances changes we discovered in *P23H-RFP/+* retinas,
811 the depletion of ELFN1 in the OPL of *P23H-RFP/+* rods was the most significant change at age
812 P30 (Fig. 5 I, Fig. 6 A-D). In our TMT-MS data, *P23H-RFP/+* ELFN1 peptide abundances were
813 also reduced at P30 and P90 (Fig. 4 C, E). Since ELFN1 localized as strings of fluorescence in
814 the ONL from P30 *P23H-RFP/+* retinas throughout Fig. 5 and Fig. 6 resulting in a significantly
815 imbalanced ELFN1 ONL/OPL distribution, we hypothesize that ELFN1 protein trafficking is
816 specifically disrupted by P23H-hRho-RFP ER aggregation. Expectedly, this ELFN1 deficit
817 coincided with significantly diminished postsynaptic mGluR6 puncta staining in the *P23H-RFP/+*
818 OPL at P30 (Fig. 6 C-D). ELFN1 and mGluR6 interact to form a critical trans-synaptic complex
819 between rod spherules and ON-type bipolar cell dendritic tips, as mGluR6 was also depleted in
820 the OPL of *Elfn1* KO mice, which also had rod spherules with no invaginating ON-type bipolar
821 cell dendrites (Cao et al., 2015).

822 Interestingly, at P90, *P23H-RFP/+* ELFN1 confocal immunofluorescence levels returned
823 to WT levels (Fig. 5 I), while Dystrophin and BASSOON levels were unchanged at P30 but then

were significantly higher in P90 *P23H-RFP/+* retinas compared to WT controls (Fig. 5 E-G, Fig. 5-1 C-D). P90 *P23H-RFP/+* rods were described as having adaptive mechanisms that enabled some degree of normal Rho trafficking to the OS and cell survival (Robichaux et al., 2022). Upregulation of presynaptic proteins may be another such mechanism used by surviving P90 *P23H-RFP/+* rods to preserve essential rod synapses in response to long-term ER disruption. In support of this, a previous study using *P23H/+* heterozygous knockin mice demonstrated synaptic transcriptome increases at age 3 months (~P90), which was attributed to homeostatic responses in rod bipolar cells to increase their sensitivity to rod input (Leinonen et al., 2020). Therefore, an adaptive strengthening of the rod-bipolar synapse may be a common phenotype in the middle stages of rod degeneration. Certain elements of the rod presynaptic machinery may be resilient to degenerating factors, since we found that the widespread ER aggregation in *P23H-RFP/+* rods caused no synaptic ribbon or vesicle docking ultrastructural defects despite the ER aggregates partially colocalizing ribbon in SIM images (Fig. 1 F-G).

In addition to ER aggregation in rods expressing P23H-hRho-RFP mutant protein, our visualization of mislocalized WT-Rho protein outlining the rod spherule plasma membrane either in WT rods overloaded with WT-Rho fusion protein (Fig. 2 K-L) or in P16 rd10 rods (Fig. 7 F, I), is informative about endogenous Rho trafficking dynamics. In our previous study, we used multiple labeling approaches with quantitative single molecule imaging to show that Rho is located throughout the IS plasma membrane in WT/non-diseased mouse rods (Haggerty et al., 2024). Thus, Rho that is overloaded in the IS may disperse throughout the entire rod plasma membrane and into the rod spherule plasma membrane including within the postsynaptic neurite invaginations. The mislocalized Rho in these overloaded regions may then be removed through endocytosis (Ropelewski and Imanishi, 2019) or exocytosis (Lewis et al., 2022), the latter of which we potentially observed here in the OPL in P16 rd10; RhoGFP/+ rods (Fig. 2 K, Fig. 7 I).

The differential impact of misfolded Rho protein ER aggregation vs. Rho overloading the rod plasma membrane is a crucial research question for future studies in order to better define the cellular status of rods in pre-degenerating disease states when they may be rescued by therapeutic intervention (Kunte et al., 2012; Leinonen et al., 2020). In this study we provide an in-depth examination of P23H-Rho-RFP ER aggregation in presynaptic rod spherules and evidence that the trafficking of some rod synaptic proteins is sensitive to these ER disruptions. An essential next step will be elucidating the trafficking mechanisms used for proteins like ELFN1 and Dystroglycan, which both require precise post-translational glycosylations to properly form trans-synaptic interactions (Sato et al., 2008; Park et al., 2020). Such future studies that elaborate on the ER-secretory system for rod synaptic proteins that we describe here will provide much needed insight into subcellular disease mechanisms in rod neurons.

Figure Legends

Figure 1. Mutant P23H-hRho-RFP protein is mislocalized within the cytoplasm of rod photoreceptor presynaptic spherules. (A) Diagram depicting the layers of the mouse outer retina (RPE = retinal pigment epithelium, OS = outer segment, IS = inner segment, ONL = outer nuclear layer, OPL = outer plexiform layer) and the two types of rod spherules (R1, top; R2, bottom). Rod photoreceptors are black, and the cone photoreceptor is purple. Spherule illustrations were based on (Li et al., 2016). (B, C) Confocal z-projections of *WT-RFP/+* and *P23H-RFP/+* retinal cryosections at age (B) P30 and (C) P90. RFP fluorescence is magenta, and sections were co-stained with WGA to label OS membranes (green) and DAPI to label nuclei (blue). White arrows = mislocalized RFP in the *P23H-RFP/+* OPLs. (D) SIM super-resolution z-projections of the OPL from a P30 WT retina. Throughout the SIM data, SIM reconstructions with no deconvolution are labeled “SIM” and are directly adjacent to any SIM images with 3D deconvolution, which are labeled “SIM + 3D decon.” In the images, RIBEYE

(yellow) and PSD95 (cyan) immunolabeled rod spherules are aligned in the OPL above a cone pedicle (white arrowhead). No 1D4 Rho labeling (magenta) is present in the WT OPL. In single spherule examples, which are all sub-stack SIM z-projections, the RIBEYE+ ribbons are horseshoe-shaped structures in the lower region of the spherules. (E, F) SIM images of the OPL in a *P23H-RFP/+* retina at age P30 with the same immunolabeling as in (D). In (E) the left images include all labeling, and the right shows the 1D4 and RIBEYE channels without PSD95. Accumulations of 1D4 immunolabeling in the OPL were localized near the synaptic ribbons (white arrows). (F) Single spherule SIM examples in *P23H-RFP/+* P30 retinas. 1D4+ Rho accumulations are localized in the cytoplasm of the spherules, typically above the ribbon. In the second SIM + 3D decon. image, a gap in the aggregated 1D4+ fluorescence is indicated with a white asterisk. The far right example is a R2-type mutant spherule with 1D4 fluorescence that surrounds the nucleus (magenta arrows) and extends into the spherule cytoplasm. The SIM image without deconvolution for this example is in Fig. 1-1 Gi. (G) SIM images of *P23H-RFP/+* retinas at age P90 with the same immunolabeling as (D-F). Images of the OPL with and without PSD95 show 1D4+ OPL accumulations (white arrows) similar to those at P30. In single spherule examples, many cytoplasmic 1D4+ aggregates surround gaps in fluorescence (white asterisks). Throughout the figure scale bars match adjacent images when not labeled.

Figure 1-1, Extended Data. (A) Western blots of WT (age P77), *Rho-GFP-1D4/+* (abb: *WT-GFP/+*, age P61), and *WT-RFP/+* (age P58) retinal lysates; 2% of the total volume from 1 mouse retina was used for each lane. In *WT-GFP/+* and *WT-RFP/+* lanes, 60-65 kDa Rho-C-1D4-positive bands corresponding to the Rho-GFP/RFP fusions are larger than the ~35 kDa endogenous monomer Rho protein bands that is present in all lanes. Magenta arrow = the band corresponding to WT-hRho-RFP. (B) Western blots of WT (age P70), *WT-GFP/+* (age P67) and *WT-RFP/+* (age P58) retinal lysates after treatment with PNGase F or buffer only. Rho protein deglycosylation shifts to lower molecular weights were evident with 1D4 (Rho-C-1D4)

immunolabeling, including shifts in the WT-hRho-RFP band (magenta arrow). Na, K ATPase beta 2 (ATP1B2) deglycosylation serves as the control ("Deglycos. control"). (C) H&E stained central retina example sections from P30 WT and P30 *WT-RFP/+* retinas. In the adjacent graph, ONL density values (# of photoreceptor nuclei in an 80 µm central retina region) are plotted for P30 WT, P30 *WT-RFP/+* and P180 *WT-RFP/+*. Points = measurements from replicate mice (N=3 each condition). Bars = mean values. (D) DAPI+ nuclei per ONL column values from confocal images like in Fig. 1 A-B were plotted for *WT-RFP/+* and *P23H-RFP/+* mice at ages P30 and P90. Points = mean values. In both (C) and (D), error bars = standard deviation and significant differences were evaluated using unpaired t-tests. **P<0.01, *** P<0.001. (E) Additional SIM super-resolution images of single spherules in P30 WT mice. Small RIBEYE+ puncta (yellow) were occasionally observed in the cytoplasmic space above the ribbon (yellow arrows). (F, G) Additional SIM images from P30 *P23H-RFP/+* retinas. Single spherule examples show 1D4 accumulations in the cytoplasmic space of the mutant rod spherules. Smaller RIBEYE+ puncta signals were also observed in these mutant spherules (yellow arrows) and often colocalized with 1D4. (Gi) is the SIM image with no deconvolution corresponding to the far right SIM + 3D decon image in Fig. 1 F. (H, I) Additional SIM images from P90 (H) WT and (I) *P23H-RFP/+* mice. 1D4 immunolabeling, acquisition and intensity levels were the same between images in (H) vs. (I). Some 1D4 fluorescence (magenta) is present in the P90 WT ONL, but there is no appreciable 1D4 signal above the background in the P90 WT OPLs. (J) Single spherule SIM examples of P90 in *P23H-RFP/+* rods demonstrate that 1D4 aggregations persist in the cytoplasmic space of the mutant rod spherules. White arrows = 1D4 (magenta) aggregates localized in the *P23H-RFP/+* OPL. White asterisks = gaps in the aggregated 1D4 fluorescence in P23H-RFP/+ spherules. Throughout the figure scale bars match adjacent images when not labeled.

Figure 2. AAV overexpression of P23H-Rho and R135L-Rho in WT rods causes synaptic mislocalization. Confocal images of retinal sections from WT mice transduced with AAVs for rod-specific expression of the following Rho fusions: (A) WT-hRho-RFP, (B) P23H-hRho-RFP, (C) WT-hRho-GFP, and (D) R135L-hRho-GFP, all at 21 days post-injection (DPI). Images on left side show Rho fusion localization (magenta) in transduced rods with DAPI (blue) labeling. Right images show co-labeling with WGA (green) as a marker for OS membranes. Grayscale images are the Rho-GFP/RFP fusion channels only. Yellow arrows = mutant Rho fusion OPL mislocalization. (E, F) AAV infected retinal sections with rods overexpressing (E) WT-hRho-RFP or (F) WT-hRho-EGFP (magenta, yellow arrows). (G, H) SIM z-projection images of the OPL from 3-micron retinal cryosections from the same AAV conditions as in (A-D). Rho fusion fluorescence is (magenta), and PSD95 immunolabeling (cyan) was used to identify rod spherules. Single spherule examples (bottom) of each AAV-driven Rho fusion are shown with PSD95 co-labeling (left) and the Rho-RFP/EGFP signal only (right). In (G), white arrows indicate P23H-hRho-RFP cytoplasmic aggregates, and dashed gray lines outline the PSD95+ plasma membrane of the magnified spherules of interest. In (H), R135L-hRho-GFP mislocalization at the spherule plasma membrane (white arrowheads) and internally (yellow arrowheads) are indicated. (I, J) SIM z-projection images from thin 1-micron sections of retinas from the same AAV conditions as in (A-D). These sections were co-immunolabeled for 1D4 (magenta) and RIBEYE (yellow). White arrows = mutant Rho fusion accumulates near the synaptic ribbon. Single spherule examples from each AAV condition are enlarged below. (K) SIM super-resolution images of WT-hRho-RFP overloaded rod spherules. 1D4+ WT-hRho-RFP (magenta) was localized along the plasma membrane of the axon and spherule (white arrows) and was colocalized with the RIBEYE synaptic ribbons (yellow arrowheads). In the far-right example, 1D4+ WT-hRho-RFP appears to bud off from the presynaptic spherule (magenta arrow). (L) SIM images of WT-hRho-GFP AAV overloaded rod spherules. WT-hRho-GFP colocalizes with the PSD95+ rod spherule plasma membrane (white arrowheads) and localizes at the rod axon

plasma membrane (white arrows). OS = outer segment, IS = inner segment, ONL = outer nuclear layer, OPL = outer plexiform layer. Scale bars match adjacent images when not labeled.

Figure 3. P23H-Rho-RFP mislocalization does not cause ultrastructural defects in rod synaptic ribbons. (A) TEM images of WT rod spherules at P30. Middle image is the annotated version of the left image (magenta asterisk = mitochondrion, cyan = spherule plasma membrane, yellow = synaptic ribbon, green arrowhead = endocytosed vesicles). In the right image, ER-like membranes (orange arrows) are wrapped around the mitochondrion. (B) TEM image of a *P23H-RFP/+* rod spherule at P30. ER-like membrane stacks (orange arrow) are localized near the mitochondrion (indicated with a magenta asterisk in all panels) and extend into the cytoplasm. (C) Additional TEM images of P30 *P23H-RFP/+* rod spherules with ER-like membrane stacks (orange arrow) associated with the spherule mitochondria. (D) TEM image of a P30 *P23H-RFP/+* R2 rod spherule with ER membrane stacks (orange arrow) from the cell body cytoplasm extending into the cytoplasm of the spherule. (E) TEM images of P90 WT spherules with ER membranes (orange arrows) surrounding the mitochondria and extending into the spherule cytoplasm. (F) TEM image of a P90 *P23H-RFP/+* spherule with expanded ER (orange arrow). (G, H) Magnified examples of ER-mitochondria contact sites (white arrows) in *P23H-RFP/+* spherules at ages (G) P30 and (H) P90. ER membranes are traced in gold, the mitochondrial membranes are traced in magenta, and the plasma membranes are traced in cyan.

Figure 3-1, Extended Data. (A) TEM images of P30 WT spherules (magenta asterisks = mitochondria, green arrowheads = endocytosed vesicles). ER-like membranes (orange arrowhead) are located near the mitochondria. (B) TEM images of P30 *P23H-RFP/+* rod spherules annotated as in (A). Denser ER membranes are observed in these mutant spherules

(orange arrowheads) (C) A P30 WT R1-type rod spherule, in which ER (orange arrowheads) is observed in the axon and surrounding the spherule mitochondrion (magenta asterisk). (D) TEM image of an R2 spherule in a P90 WT retina depicting ER-like membranes (orange arrowhead) extending from around the nucleus and into the spherule of the cytoplasm.

Figure 4. Photoreceptor and synaptic protein abundance changes are found in *P23H-RFP/+* retinas with TMT-MS proteomics. (A) Diagram of the front view of a rod spherule and a magnified view of the active zone and the synaptic cleft to highlight the approximate localizations of rod synaptic proteins including key trans-synaptic protein complexes. (B) Volcano plot of TMT-MS relative peptide abundances for select photoreceptor and synaptic proteins (based on Gene Ontology Cellular Component classification, see Methods) in age P30 *P23H-RFP/+* vs WT retinas. X axis = Log_2 fold change values with a significance threshold of 0.2, Y-axis = p-values (-Log10) with a significance threshold of 1.5. Green points represent protein targets above the thresholds and magenta points are targets below the thresholds. Annotated protein names are based on FASTA gene names. (C) Graph of select relative protein abundances from the P30 TMT-MS data in Fig. 4-1 B. WT (open circles) were normalized to 1 and superimposed with *P23H-RFP/+* values (black diamonds). Magenta asterisks = significant downregulation, and green asterisks = significant upregulation based on adjusted p-values from unpaired t-tests. Bars = mean values, error bars = standard deviations. Asterisks indicate the following adjusted p-values: * P < 0.055, *** P<0.001. (D) TMT-MS volcano plot comparing relative peptide abundances in age P90 *P23H-RFP/+* and WT retinas for the same protein list and plot parameters as in (B). (E) Graph of select relative protein abundances from the P90 TMT-MS data in Fig 4-1 B with the same normalization and formatting as in (C). Asterisks indicate the following adjusted p-values: * P <0.055, ** P<0.01, *** P<0.001.

Figure 4-1, Extended Data. (A) SIM super-resolution image of the OPL of a P30 WT retina. The rod synaptic protein ELFN1 (cyan) is typically located beneath the synaptic ribbon (yellow). Gaps in a single ELFN1 fluorescent punctum suggest the shape of invaginating post-synaptic neurites (dotted white lines). (B) Table of normalized TMT-MS values for select proteins, including the proteins in Fig. 4 B and D. Dag1 = Dystroglycan. (C) Western blot analysis for Dystrophin isoforms in WT and *P23H-RFP/+* whole retinas at ages P30 and P90. Each lane represents a retinal lysate sample from a separate mouse. Colored brackets on the blots correspond to the colored bars in the graphs for densitometry intensity quantification. All intensities are plotted as normalized to corresponding tubulin band intensities (Tubb5, bottom blots).

Figure 5. Quantitative confocal imaging analysis of synaptic protein abundance changes in *P23H-RFP/+* mice. (A, B) Example confocal z-projections from WT and *P23H-RFP/+* retinal cryosections at (A) P30 and (B) P90 focused on regions of the lower/proximal ONL and OPL with Dystrophin (cyan) and BASSOON (Bsn, yellow) immunolabeling and DAPI counterstaining (blue). RFP acquisition and intensity levels were matched between WT and *P23H-RFP/+* samples, and RFP fluorescence (magenta) was detectable only in the ONL and OPL of the *P23H-RFP/+* sections. (C, D) Confocal z-projections for WT and *P23H-RFP/+* retinal cryosections at (C) P30 and (D) P90 with ELFN1 immunolabeling (green) and DAPI nuclear staining (blue). RFP fluorescence (magenta) was again only detected in the *P23H-RFP/+* images. (E, F) Graphs of normalized puncta intensity values for (E) Dystrophin and (F) BASSOON from confocal images of WT and *P23H-RFP/+* retinas at P30 and P90. Graphs are aggregated data from replicate WT vs. *P23H-RFP/+* puncta intensity comparisons; for each comparison, values were normalized to WT mean = 1, and all replicates were aggregated. In the graphs, WT values are open circles and *P23H-RFP/+* are closed circles. Bars = aggregated means and error bars = standard deviations after error propagation. Asterisks are based on

unpaired t-tests: * P <0.05, ** P<0.01. (G) Time course plot of Dystrophin (blue) and Bassoon (yellow) normalized (Norm.) puncta intensity measurements from *P23H-RFP/+* retinas. For all time points, the plotted *P23H-RFP/+* aggregate values are normalized to a WT mean = 1, and the P30 and P90 data are the same aggregated replicates as in (E) and (F). Asterisks represent the same statistical differences plotted for the P90 data in (E) and (F). (H) Time course plot of DAPI+ photoreceptor nuclei per column counted from both WT and *P23H-RFP/+* in confocal images analyzed throughout the puncta analyses in (E - G). Black circles = WT nuclei counts. Pink diamonds = *P23H-RFP/+* nuclei counts. One phase exponential decay curve fits were added in GraphPad Prism. (I) Graph of normalized ELFN1 OPL intensities between WT and *P23H-RFP/+* retinas at ages P30 and P90. The data were normalized and aggregated as in (E) and (F). ** P < 0.01, based on an unpaired t-test. (J) Example confocal images from *P23H-RFP/+* retinas depicting RFP fluorescence (magenta) colocalized with either Dystrophin (top, green) or BASSOON (Bsn, bottom, green) immunolabeling. In magnified views, on the right, Dystrophin and Bsn intensities are heat map pseudocolored and superimposed with the RFP signal as white outlines. White arrows indicate RFP+ Dystrophin/Bassoon colocalizations and yellow arrows indicate RFP- Dystrophin/Bassoon examples. (K) Graph of replicate puncta intensity values from the P90 *P23H-RFP/+* RFP colocalization assay for Dystrophin (cyan) BASSOON (yellow). Unfilled bars indicate the range of RFP- values and striped bars indicate the range of RFP^{+} values. The middle lines in each bar represent mean values. For all replicates, values were normalized to WT mean = 1. Asterisks are based on unpaired t-tests: * P <0.05, ** P<0.01.

Figure 5-1, Extended Data. (A, B) Example confocal z-projections of WT (left) and *P23H-RFP/+* (right) retinas immunolabeled for ELFN1 (green) at ages (A) P30 or (B) P90. ELFN1 and RFP (magenta) levels were matched between WT and *P23H-RFP/+* images. Yellow arrows = strings of ELFN1 in the *P23H-RFP/+* ONL. The ELFN1 only channel is shown in grayscale. (C,

D) Graphs corresponding to the data in Fig. 5 G. (C) Time course analysis of Dystrophin (cyan) normalized intensities ranging from age P14 to P365 in WT (open circle) and *P23H-RFP/+* (closed circle) retinas. Asterisks are as follows: P <0.05 *, P<0.01 **, P<0.001*** (unpaired t-tests). (D) Time course analysis of BASSOON (yellow) normalized intensities ranging from age P14 to P365 in WT (open circle) and *P23H-RFP/+* (closed circle) retinas. Asterisks are as follows: P <0.05 *, P<0.01 **, P<0.001*** (unpaired t-tests). (E) Graph of aggregated and normalized data corresponding to the P90 RFP colocalization data in Fig 5 K as well as the P30 data. Dystrophin values are cyan, and BASSOON values are yellow.

Figure 6. ELFN1 protein distribution is altered in *P23H-RFP/+* retinas. (A, B) Confocal z-projection images of a (A) P30 WT (B) P30 *P23H-RFP/+* retinal cryosections immunolabeled for ELFN1 (green) and mGluR6 (magenta) and counterstained for DAPI (blue). Grayscale images depict the ELFN1 and mGluR6 channels separately. (C) Magnified confocal images with the same labeling focused on smaller portions of the OPL. ELFN1 and mGluR6 staining, acquisition and intensity settings were matched throughout (A-C) between the P30 WT and P30 *P23H-RFP/+* sections. (D) Normalized intensity graph (left side) based on layer-specific intensity measurements for ELFN1 (green) and mGluR6 (magenta). Values were aggregated from replicate WT vs. P*23H-RFP/+* experiments and normalized to WT mean = 1; WT mean values are represented as circles and *P23H-RFP/+* values are triangles. On the right, ratios of ELFN1 intensity ONL/OPL intensities are plotted with the same parameters. All bars = aggregated mean values, error bars = standard deviations after error propagation. Asterisks are based on unpaired t-tests p-values as follows: * P <0.05, *** P<0.001. ns = not significant. (E) Example RNAscope SIM z-projections images for *Elfn1* mRNA (green) in P30 WT and P30 *P23H-RFP/+* retinas, alongside example SIM images probed for *POLR2A* (positive control) and *dapB* (negative control) mRNAs. Sections were co-immunolabeled for centrin (magenta) to label connecting cilia and counterstained with DAPI (blue). Grayscale images of mRNA puncta are

shown to the right of the merged images. Yellow dotted lines = the IS:ONL and ONL:OPL boundaries based on the DAPI staining. (F, G) SIM z-projection images of (F) P30 WT and (G) P30 *P23H-RFP/+* retinas immunolabeled for Sec61β (ER-marker, magenta), PSD95 (cyan), and BASSOON (yellow). Sec61β is localized throughout the layers of the photoreceptors (left), and in magnified images, the PSD95 rod spherule border is annotated in select rod spherules to demonstrate Sec61β+ ER fluorescence within individual WT and *P23H-RFP/+* rod spherules (white arrowheads). In the *P23H-RFP/+* image in (G), IS ER aggregations are labeled with yellow arrows. OS = outer segment, IS = inner segment, ONL = outer nuclear layer, OPL = outer plexiform layer. Scalebars match adjacent images when not labeled.

Figure 6-1, Extended Data. (A, B) Additional confocal z-projection images of (A) P30 WT and (B) P30 P23H-RFP/+ retinal cryosections immunolabeled for ELFN1 (green), mGluR6 (magenta), and DAPI (blue). Merged images are adjacent to grayscale images of the separated ELFN1 and mGluR6 channels. (C) Graph depicting aggregated and normalized *Elfn1* mRNA particles per area (μm^2) from the RNAScope examples data in Fig. 6 E. *Elfn1* counts are graphed for the IS, dONL, pONL, and OPL layers from P30 WT (circles) and P30 P23H-RFP/+ (triangles) retinas. Values are from replicate WT vs *P23H-RFP/+* comparisons and all data were normalized to WT mean = 1. * P <0.05 based on unpaired t-tests. (D) Graph of the de-aggregated, normalized Elfn1 mRNA particles per area data corresponding to Fig. 6-1 C. (E) Graph of replicate, normalized mRNA particles per area values for the control RNAscope probes in Fig. 6E. *P < 0.05, *** P<0.001 are based on unpaired t-tests. In all graphs: bars = aggregate mean aggregate values, error bars = standard deviations after error propagation.

Figure 7. Rho mislocalization in rd10 RP mutant retinas does not alter rod synaptic protein levels. (A, B) Confocal z-projections of retinal cryosections from WT and rd10 mice at age P16 (A) or P20 (B). Sections were immunolabeled with the 4D2 Rho antibody (Rho,

magenta) and counterstained with DAPI (blue). Rho only images are in grayscale. Mislocalized 4D2+ Rho signal is present in the rd10 OPLs (white arrows). (C) SIM images of a P16 WT retina immunolabeled for 4D2 (Rho, magenta), RIBEYE (yellow), and PSD95 (cyan). Rho fluorescence was detected throughout the OS, IS, and ONL but not in the OPL based on images with (left) and without (right) the PSD95 channel. (D) SIM image of a P16 rd10 retina labeled as in (C). Rho fluorescence was detected throughout the OS, IS, ONL, and also mislocalized in the OPL (white arrows) based on images with (left) and without (right) PSD95. The Rho channel only is in grayscale. 4D2 Rho immunolabeling, acquisition settings and intensity levels were matched between (C) and (D). (E) SIM images of the OPL in WT and rd10 mice at ages P16 and P20 with the same labeling and colors as in (C-D). 4D2+ Rho staining, acquisition and intensity settings were matched between all conditions, and in the WT OPL, the 4D2 signal is not consistently above background levels. In rd10 retinas at ages P16 and P20, mislocalized 4D2+ Rho labeling in the OPL is colocalized with PSD95 (top row) and surrounds the ribbons; Rho mislocalization in the P20 rd10 OPL is not as evident as at P16. (F) Magnified single rod spherule SIM images from P16 rd10 retinas with the same labeling as in (E). Mislocalized Rho colocalizes with PSD95 at the spherule plasma membrane (left images) and surrounds the ribbon (right images, no PSD95 channel). (G) Confocal z-projections of cryosections from $Rho^{GFP/+}$ (left) and rd10; $Rho^{GFP/+}$ (right) retinas depicting Rho-GFP (GFP, green) localization. Sections were counterstained with DAPI (blue). Grayscale images are GFP only with increased brightness to demonstrate Rho-GFP OPL mislocalization in rd10; $Rho^{GFP/+}$ retinas (white arrows). (H) SIM image of a P16 rd10; $Rho^{GFP/+}$ retinal cryosection immunolabeled for RIBEYE (magenta) to demonstrate that mislocalized Rho-GFP in the OPL overlaps with RIBEYE+ ribbons. (I) SIM images of thin resin sections of P16 rd10; $Rho^{GFP/+}$ retinas that were co-immunolabeled with a GFP nanobody (NbGFP-A647, magenta) and for RIBEYE (yellow). NbGFP-A647 labeling was specific for Rho-GFP in these sections as cone ribbons are present (white arrowheads) with no surrounding NbGFP-A647 signal. In magnified views of rd10;

Rho$^{GFP/+}$ spherules, Rho-GFP is localized in the OPL along the spherule plasma membranes surrounding the ribbons (white arrows). Small Rho-GFP puncta were observed in the OPL extracellular space as if detached from the spherule membrane (green arrowheads). (J) Graph of aggregated normalized puncta intensities for Dystrophin (cyan) and BASSOON (Bsn, yellow) from age P16 and P20 WT (open circles) and rd10 (closed circles) retinas. Values were normalized to WT mean = 1. Bars indicate the aggregate means from replicate WT vs. rd10 comparisons, and error bars = standard deviation after error propagation. There were no significant differences based on unpaired t-tests. OS = outer segment, IS = inner segment, ONL = outer nuclear layer, OPL = outer plexiform layer. Scalebars match adjacent images when not labeled.

Figure 7-1, Extended Data. (A) SIM super-resolution example images of P20 WT (left) and rd10 (right) retinas. 4D2+ Rho signal (magenta) is localized in WT rods at the bottom of the ONL near the spherules (cyan) and ribbons (yellow), but not in the OPL. Faint 4D2 staining in rd10 rods is detectable in the OPL. (B) 4D2+ Rho fluorescence in a SIM super-resolution image of a P16 WT retina. Rho is located along the IS plasma membrane (yellow arrows). (C) 4D2+ Rho fluorescence in SIM super-resolution example images of P16 rd10 retinas demonstrates Rho localization at the IS plasma membrane and myoid region. (D) More 4D2+ Rho fluorescence in SIM super-resolution images from P16 WT and rd10 retinas focused on the ONL. Here, Rho is localized along the membranes of rod outer fibers/axons. (E) SIM super-resolution single spherule example images from P16 rd10 retinas. 4D2+ Rho (magenta) is colocalized with PSD95 (cyan) at the spherule plasma membrane and along rod axons (white arrows). (F) SIM super-resolution single spherule images from P16 WT retinas. 4D2+ Rho staining, acquisition and intensities were matched to all the examples in (E), (F), and Fig. 7 F. There is only sporadic, faint Rho (magenta) signal in some WT examples.

Figure 8. Diagram model of ER protein secretion in WT rod spherules and the impact of Rho mislocalization in mutant rod spherules. (A) Diagram of a WT rod spherule. The spherule plasma membrane is highlighted in cyan. ER (gold) wraps around the mitochondrion (tan) in the cytoplasmic space above the synaptic ribbon (yellow). Trans-synaptic cell adhesion proteins (green) align the synaptic cleft with the postsynaptic neurites (ON-type bipolar cells: orange; horizontal cells: black). These proteins (green) are potentially trafficked and turned over by an ER secretory pathway that extends to the rod spherule cytoplasm. (B) Diagram of a *P23H-RFP/+* rod spherule. Mutant Rho (magenta dots) aggregates in expanded ER (gold) in the cytoplasmic space of spherules, blocking the normal secretion of synaptic proteins. (C) Diagram of a rd10 rod spherule or a WT spherule with over-expressed WT-Rho fusion protein or mutant R135L-hRho-GFP protein. In these cases, Rho (magenta) mislocalizes along the spherule plasma membrane (cyan) such that the ER (gold) is putatively unaffected, and thus synaptic protein trafficking is normal.

References

Adly MA, Spiwoks I, Vollrath L (1999) Ultrastructural Changes of Photoreceptor Synaptic Ribbons in Relation to Time of Day and Illumination. 40.

Agosto MA, Adeosun AAR, Kumar N, Wensel TG (2021) The mGluR6 ligand-binding domain, but not the C-terminal domain, is required for synaptic localization in retinal ON-bipolar cells. J Biol Chem 297.

Agrawal SA, Burgoyne T, Eblimit A, Bellingham J, Parfitt DA, Lane A, Nichols R, Asomugha C, Hayes MJ, Munro PM, Xu M, Wang K, Futter CE, Li Y, Chen R, Cheetham ME (2017) REEP6 deficiency leads to retinal degeneration through disruption of ER homeostasis and protein trafficking. Hum Mol Genet 26:2667–2677.

Aguilà M, Bevilacqua D, McCulley C, Schwarz N, Athanasiou D, Kanuga N, Novoselov SS, Lange CAK, Ali RR, Bainbridge JW, Gias C, Coffey PJ, Garriga P, Cheetham ME (2014) Hsp90 inhibition protects against inherited retinal degeneration. Hum Mol Genet 23:2164–2175.

1185 Athanasiou D, Aguila M, Bellingham J, Li W, McCulley C, Reeves PJ, Cheetham ME (2018) The
1186 molecular and cellular basis of rhodopsin retinitis pigmentosa reveals potential strategies
1187 for therapy. Prog Retin Eye Res 62:1–23.

1188 Babai N, Morgans CW, Thoreson WB (2010) Calcium-induced calcium release contributes to
1189 synaptic release from mouse rod photoreceptors. Neuroscience 165:1447–1456.

1190 Barhoum R, Martínez-Navarrete G, Corrochano S, Germain F, Fernandez-Sanchez L, De La
1191 Rosa EJ, De La Villa P, Cuenca N (2008) Functional and structural modifications during
1192 retinal degeneration in the rd10 mouse. Neuroscience 155:698–713.

1193 Behrens C, Schubert T, Haverkamp S, Euler T, Berens P (2016) Connectivity map of bipolar
1194 cells and photoreceptors in the mouse retina. eLife 5:1–20.

1195 Beltran WA, Hammond P, Acland GM, Aguirre GD (2006) A frameshift mutation in RPGR exon
1196 ORF15 causes photoreceptor degeneration and inner retina remodeling in a model of X-
1197 linked retinitis pigmentosa. Invest Ophthalmol Vis Sci 47:1669–1681.

1198 Broadwell RD, Cataldo AM (1984) The neuronal endoplasmic reticulum: Its cytochemistry and
1199 contribution to the endomembrane system. II. Axons and terminals. J Comp Neurol
1200 230:231–248.

1201 Cao Y, Sarria I, Fehlhaber KE, Kamasawa N, Orlandi C, James KN, Hazen JL, Gardner MR,
1202 Farzan M, Lee A, Baker S, Baldwin K, Sampath AP, Martemyanov KA (2015) Mechanism
1203 for Selective Synaptic Wiring of Rod Photoreceptors into the Retinal Circuitry and Its
1204 Role in Vision. Neuron 87:1248–1260.

1205 Cao Y, Wang Y, Dunn HA, Orlandi C, Shultz N, Kamasawa N, Fitzpatrick D, Li W, Zeitz C,
1206 Hauswirth W, Martemyanov KA (2020) Interplay between cell-adhesion molecules
1207 governs synaptic wiring of cone photoreceptors. Proc Natl Acad Sci 117:23914–23924.

1208 Carter-Dawson LD, Lavail MM (1979) Rods and cones in the mouse retina. I. Structural analysis
1209 using light and electron microscopy. J Comp Neurol 188:245–262.

1210 Chen M, Križaj D, Thoreson WB (2014) Intracellular calcium stores drive slow non-ribbon
1211 vesicle release from rod photoreceptors. Front Cell Neurosci 8.

1212 Chen M, Van Hook MJ, Thoreson WB (2015) Ca2+ Diffusion through Endoplasmic Reticulum
1213 Supports Elevated Intraterminal Ca2+ Levels Needed to Sustain Synaptic Release from
1214 Rods in Darkness. J Neurosci 35:11364–11373.

1215 Chuang J-Z, Vega C, Jun W, Sung C-H (2004) Structural and functional impairment of endocytic
1216 pathways by retinitis pigmentosa mutant rhodopsin-arrestin complexes. J Clin Invest
1217 114:131–140.

1218 Dick O, Tom Dieck S, Altrock WD, Ammermüller J, Weiler R, Garner CC, Gundelfinger ED,
1219 Brandstätter JH (2003) The Presynaptic Active Zone Protein Bassoon Is Essential for
1220 Photoreceptor Ribbon Synapse Formation in the Retina. Neuron 37:775–786.

1221 Fariss RN, Li ZY, Milam AH (2000) Abnormalities in rod photoreceptors, amacrine cells, and
1222 horizontal cells in human retinas with retinitis pigmentosa. Am J Ophthalmol 129:215–
1223 223.

1224 Fariss RN, Molday RS, Fisher SK, Matsumoto B (1997) Evidence from normal and degenerating
1225 photoreceptors that two outer segment integral membrane proteins have separate
1226 transport pathways. J Comp Neurol 387:148–156.

1227 Fisher SK, Lewis GP, Linberg KA, Verardo MR (2005) Cellular remodeling in mammalian retina:
1228 Results from studies of experimental retinal detachment. Prog Retin Eye Res 24:395–
1229 431.

1230 Flannery JG, Zolotukhin S, Vaquero MI, LaVail MM, Muzyczka N, Hauswirth WW (1997)
1231 Efficient photoreceptor-targeted gene expression in vivo by recombinant adeno-
1232 associated virus. Proc Natl Acad Sci U S A 94:6916–6921.

1233 Fuchs M, Brandstätter JH, Regus-Leidig H (2014) Evidence for a Clathrin-independent mode of
1234 endocytosis at a continuously active sensory synapse. Front Cell Neurosci 8 Available
1235 at: http://journal.frontiersin.org/article/10.3389/fncel.2014.00060/abstract [Accessed
1236 November 2, 2023].

1237 Furukawa T, Ueno A, Omori Y (2020) Molecular mechanisms underlying selective synapse
1238 formation of vertebrate retinal photoreceptor cells. Cell Mol Life Sci 77:1251–1266.

1239 Gargini C, Terzibasi E, Mazzoni F, Strettoi E (2007) Retinal organization in the retinal
1240 degeneration 10 (rd10) mutant mouse: A morphological and ERG study. J Comp Neurol
1241 500:222–238.

1242 Goedhart J, Luijsterburg MS (2020) VolcaNoseR is a web app for creating, exploring, labeling
1243 and sharing volcano plots. Sci Rep 10:20560.

1244 Grabner CP, Gandini MA, Rehak R, Le Y, Zamponi GW, Schmitz F (2015) RIM1/2-Mediated
1245 Facilitation of Cav1.4 Channel Opening Is Required for Ca^{2+} -Stimulated Release in
1246 Mouse Rod Photoreceptors. J Neurosci 35:13133–13147.

1247 Grossman GH, Pauer GJT, Narendra U, Peachey NS, Hagstrom SA (2009) Early Synaptic
1248 Defects in *tulp1* $^{-/-}$ Mice. Investig Opthalmology Vis Sci 50:3074.

1249 Guo D, Ru J, Xie L, Wu M, Su Y, Zhu S, Xu S, Zou B, Wei Y, Liu X, Liu Y, Liu C (2022)
1250 Tmem138 is localized to the connecting cilium essential for rhodopsin localization and
1251 outer segment biogenesis. Proc Natl Acad Sci 119:e2109934119.

1252 Haggerty KN, Eshelman SC, Sexton LA, Frimpong E, Rogers LM, Agosto MA, Robichaux MA
1253 (2024) Super-resolution mapping in rod photoreceptors identifies rhodopsin trafficking
1254 through the inner segment plasma membrane as an essential subcellular pathway.
1255 Baden T, ed. PLoS Biol 22:e3002467.

1256 Hagstrom SA, Adamian M, Scimeca M, Pawlyk BS, Yue G, Li T (2001) A role for the Tubby-like
1257 protein 1 in rhodopsin transport. Invest Ophthalmol Vis Sci 42:1955–1962.

1258 Hagstrom SA, Duyao M, North MA, Li T (1999) Retinal Degeneration in tulp1 −/− Mice: Vesicular
1259 Accumulation in the Interphotoreceptor Matrix. 40.

1260 Hicks D, Molday RS (1986) Differential immunogold-dextran labeling of bovine and frog rod and
1261 cone cells using monoclonal antibodies against bovine rhodopsin. Exp Eye Res 42:55–
1262 71.

1263 Hsu Y-C, Chuang J-Z, Sung C-H (2015) Light Regulates the Ciliary Protein Transport and Outer
1264 Segment Disc Renewal of Mammalian Photoreceptors. Dev Cell 32:731–742.

1265 Jae SA, Ahn KN, Kim JY, Seo JH, Kim HK, Goo YS (2013) Electrophysiological and Histologic
1266 Evaluation of the Time Course of Retinal Degeneration in the *rd10* Mouse Model of
1267 Retinitis Pigmentosa. Korean J Physiol Pharmacol 17:229.

1268 Johnson JE, Perkins GA, Giddabasappa A, Chaney S, Xiao W, White AD, Brown JM, Waggoner
1269 J, Ellisman MH, Fox DA (2007) Spatiotemporal regulation of ATP and Ca2+ dynamics in
1270 vertebrate rod and cone ribbon synapses. Mol Vis 13:887–919.

1271 Kaushal S, Khorana HG (1994) Structure and Function in Rhodopsin. 7. Point Mutations
1272 Associated with Autosomal Dominant Retinitis Pigmentosa. Biochemistry 33:6121–6128.

1273 Kesharwani A, Schwarz K, Dembla E, Dembla M, Schmitz F (2021) Early Changes in Exo- and
1274 Endocytosis in the EAE Mouse Model of Multiple Sclerosis Correlate with Decreased
1275 Synaptic Ribbon Size and Reduced Ribbon-Associated Vesicle Pools in Rod
1276 Photoreceptor Synapses. Int J Mol Sci 22:10789.

1277 Konietzny A, Wegmann S, Mikhaylova M (2023) The endoplasmic reticulum puts a new spin on
1278 synaptic tagging. Trends Neurosci 46:32–44.

1279 Koulen P, Fletcher EL, Craven SE, Bredt DS, Wässle H (1998) Immunocytochemical
1280 Localization of the Postsynaptic Density Protein PSD-95 in the Mammalian Retina. J
1281 Neurosci 18:10136–10149.

1282 Krizaj D (2005) Serca isoform expression in the mammalian retina. Exp Eye Res 81:690–699.

1283 Križaj D (2012) Calcium stores in vertebrate photoreceptors. Adv Exp Med Biol 740:873–889.

1284 Kunte MM, Choudhury S, Manheim JF, Shinde VM, Miura M, Chiodo VA, Hauswirth WW,
1285 Gorbatyuk OS, Gorbatyuk MS (2012) ER Stress Is Involved in T17M Rhodopsin-Induced
1286 Retinal Degeneration. Investig Opthalmology Vis Sci 53:3792.

1287 Ladman AJ (1958) The fine structure of the rod-bipolar cell synapse in the retina of the albino
1288 rat. J Biophys Biochem Cytol 4:459–466.

1289 Lee A, Wang S, Williams B, Hagen J, Scheetz TE, Haeseleer F (2015) Characterization of
1290 Cav1.4 Complexes (α11.4, β2, and α2δ4) in HEK293T Cells and in the Retina. J Biol
1291 Chem 290:1505–1521.

1292 Lee S, Tan HY, Geneva II, Kruglov A, Calvert PD (2018) Actin filaments partition primary cilia
1293 membranes into distinct fluid corrals. J Cell Biol 217:2831–2849.

1294 Leinonen H, Pham NC, Boyd T, Santoso J, Palczewski K, Vinberg F (2020) Homeostatic
1295 plasticity in the retina is associated with maintenance of night vision during retinal
1296 degenerative disease. eLife 9:e59422.

1297 Lem J, Krasnoperova NV, Calvert PD, Kosaras B, Cameron DA, Nicolò M, Makino CL, Sidman
1298 RL (1999) Morphological, physiological, and biochemical changes in rhodopsin knockout
1299 mice. Proc Natl Acad Sci 96:736–741.

1300 Lewis TR, Phan S, Kim K-Y, Jha I, Castillo CM, Ding J-D, Sajdak BS, Merriman DK, Ellisman
1301 MH, Arshavsky VY (2022) Microvesicle release from inner segments of healthy
1302 photoreceptors is a conserved phenomenon in mammalian species. Dis Model Mech
1303 15:dmm049871.

1304 Li S, Mitchell J, Briggs DJ, Young JK, Long SS, Fuerst PG (2016) Morphological Diversity of the
1305 Rod Spherule: A Study of Serially Reconstructed Electron Micrographs Barnes S, ed.
1306 PLOS ONE 11:e0150024.

1307 Lindsey J, Ellisman M (1985) The neuronal endomembrane system. III. The origins of the
1308 axoplasmic reticulum and discrete axonal cisternae at the axon hillock. J Neurosci
1309 5:3135–3144.

1310 Lovas B (1971) Tubular networks in the terminal endings of the visual receptor cells in the
1311 human, the monkey, the cat and the dog. Z Für Zellforsch Mikrosk Anat 121:341–357.

1312 Mercurio AM, Holtzman E (1982) Smooth endoplasmic reticulum and other agranular reticulum
1313 in frog retinal photoreceptors. J Neurocytol 11:263–293.

1314 Milam AH, Li ZY, Fariss RN (1998) Histopathology of the human retina in retinitis pigmentosa.
1315 Prog Retin Eye Res 17:175–205.

1316 Molday RS, MacKenzie D (1983) Monoclonal antibodies to rhodopsin: characterization, cross-
1317 reactivity, and application as structural probes. Biochemistry 22:653–660.

1318 Moser T, Grabner CP, Schmitz F (2020) Sensory Processing at Ribbon Synapses in the Retina
1319 and the Cochlea. Physiol Rev 100:103–144.

1320 Omori Y, Araki F, Chaya T, Kajimura N, Irie S, Terada K, Muranishi Y, Tsujii T, Ueno S, Koyasu T,
1321 Tamaki Y, Kondo M, Amano S, Furukawa T (2012) Presynaptic Dystroglycan–Pikachurin
1322 Complex Regulates the Proper Synaptic Connection between Retinal Photoreceptor and
1323 Bipolar Cells. J Neurosci 32:6126–6137.

1324 Orlandi C, Omori Y, Wang Y, Cao Y, Ueno A, Roux MJ, Condomitti G, De Wit J, Kanagawa M,
1325 Furukawa T, Martemyanov KA (2018) Transsynaptic Binding of Orphan Receptor
1326 GPR179 to Dystroglycan-Pikachurin Complex Is Essential for the Synaptic Organization
1327 of Photoreceptors. Cell Rep 25:130-145.e5.

1328 Park D ha, Park S, Song J man, Kang M, Lee S, Horak M, Suh YH (2020) N-linked glycosylation
1329 of the mGlu7 receptor regulates the forward trafficking and transsynaptic interaction with
1330 Elfn1. FASEB J 34:14977–14996.

1331 Pawlyk BS, Smith AJ, Buch PK, Adamian M, Hong D-H, Sandberg MA, Ali RR, Li T (2005) Gene
1332 Replacement Therapy Rescues Photoreceptor Degeneration in a Murine Model of Leber
1333 Congenital Amaurosis Lacking RPGRIP. Investig Opthalmology Vis Sci 46:3039.

1334 Robichaux MA, Nguyen V, Chan F, Kailasam L, He F, Wilson JH, Wensel TG (2022) Subcellular
1335 localization of mutant P23H rhodopsin in an RFP fusion knock-in mouse model of
1336 retinitis pigmentosa. Dis Model Mech 15:dmm049336.

1337 Roof DJ, Adamian M, Hayes A (1994) Rhodopsin Accumulation at Abnormal Sites in Retinas of
1338 Mice With a Human P23H Rhodopsin Transgene. 35.

1339 Ropelewski P, Imanishi Y (2019) Disrupted Plasma Membrane Protein Homeostasis in a
1340 *Xenopus Laevis* Model of Retinitis Pigmentosa. J Neurosci 39:5581–5593.

1341 Sakami S, Maeda T, Bereta G, Okano K, Golczak M, Sumaroka A, Roman AJ, Cideciyan AV,
1342 Jacobson SG, Palczewski K (2011) Probing Mechanisms of Photoreceptor Degeneration
1343 in a New Mouse Model of the Common Form of Autosomal Dominant Retinitis
1344 Pigmentosa due to P23H Opsin Mutations. J Biol Chem 286:10551–10567.

1345 Saliba RS, Munro PMG, Luthert PJ, Cheetham ME (2002) The cellular fate of mutant rhodopsin:
1346 Quality control, degradation and aggresome formation. J Cell Sci 115:2907–2918.

1347 Sato S, Omori Y, Katoh K, Kondo M, Kanagawa M, Miyata K, Funabiki K, Koyasu T, Kajimura N,
1348 Miyoshi T, Sawai H, Kobayashi K, Tani A, Toda T, Usukura J, Tano Y, Fujikado T,
1349 Furukawa T (2008) Pikachurin, a dystroglycan ligand, is essential for photoreceptor
1350 ribbon synapse formation. Nat Neurosci 11:923–931.

1351 Schindelin J, Arganda-Carrera I, Frise E, Verena K, Mark L, Tobias P, Stephan P, Curtis R,
1352 Stephan S, Benjamin S, Jean-Yves T, Daniel JW, Volker H, Kevin E, Pavel T, Albert C
1353 (2009) Fiji - an Open platform for biological image analysis. Nat Methods 9.

1354 Schmitz F, Königstorfer A, Südhof TC (2000) RIBEYE, a component of synaptic ribbons: A
1355 protein's journey through evolution provides insight into synaptic ribbon function. Neuron
1356 28:857–872.

1357 Schmitz F, Natarajan S, Venkatesan JK, Wahl S, Schwarz K, Grabner CP (2012) EF hand-
1358 mediated Ca2+- signalling in photoreceptor synaptic terminals. Front Mol Neurosci.

1359 Sechrest ER, Ma X, Cahill ME, Barbera RJ, Wang Y, Deng W-T (2024) Structural and functional
1360 rescue of cones carrying the most common cone opsin C203R missense mutation. JCI
1361 Insight 9:e172834.

1362 Spacek J, Harris KM (1996) Three-Dimensional Organization of Smooth Endoplasmic Reticulum
1363 in Hippocampal CA1 Dendrites and Dendritic Spines of the Immature and Mature Rat.

1364 Sung CH, Makino C, Baylor D, Nathans J (1994) A rhodopsin gene mutation responsible for
1365 autosomal dominant retinitis pigmentosa results in a protein that is defective in
1366 localization to the photoreceptor outer segment. J Neurosci 14:5818–5833.

Sung CH, Schneider BG, Agarwal N, Papermaster DS, Nathans J (1991) Functional heterogeneity of mutant rhodopsins responsible for autosomal dominant retinitis pigmentosa. Proc Natl Acad Sci 88:8840–8844.

Torten G, Fisher SK, Linberg KA, Luna G, Perkins G, Ellisman MH, Williams DS (2023) Three-Dimensional Ultrastructure of the Normal Rod Photoreceptor Synapse and Degenerative Changes Induced by Retinal Detachment. J Neurosci 43:5468–5482.

Townes-Anderson E, Dacheux RF, Raviolal E (1988) Rod Photoreceptors Dissociated from the Adult Rabbit Retina.

Tsuboi M, Hirabayashi Y (2021) New insights into the regulation of synaptic transmission and plasticity by the endoplasmic reticulum and its membrane contacts. Proc Jpn Acad Ser B Phys Biol Sci 97:559–572.

Vasudevan S, Senapati S, Pendergast M, Park PS –H (2024) Aggregation of rhodopsin mutants in mouse models of autosomal dominant retinitis pigmentosa. Nat Commun 15.

Wang K, Xiao J, Peng B, Xing F, So K-F, Tipoe GL, Lin B (2015) Retinal structure and function preservation by polysaccharides of wolfberry in a mouse model of retinal degeneration. Sci Rep 4:7601.

Wersinger E, Bordais A, Schwab Y, Sene A, Bénard R, Alunni V, Sahel JA, Rendon A, Roux MJ (2011) Reevaluation of dystrophin localization in the mouse retina. Invest Ophthalmol Vis Sci 52:7901–7908.

Wu Y, Whiteus C, Xu CS, Hayworth KJ, Weinberg RJ, Hess HF, De Camilli P (2017) Contacts between the endoplasmic reticulum and other membranes in neurons. Proc Natl Acad Sci 114 Available at: https://pnas.org/doi/full/10.1073/pnas.1701078114 [Accessed November 2, 2023].

Zhao L, Zabel MK, Wang X, Ma W, Shah P, Fariss RN, Qian H, Parkhurst CN, Gan W, Wong WT (2015) Microglial phagocytosis of living photoreceptors contributes to inherited retinal degeneration. EMBO Mol Med 7:1179–1197.

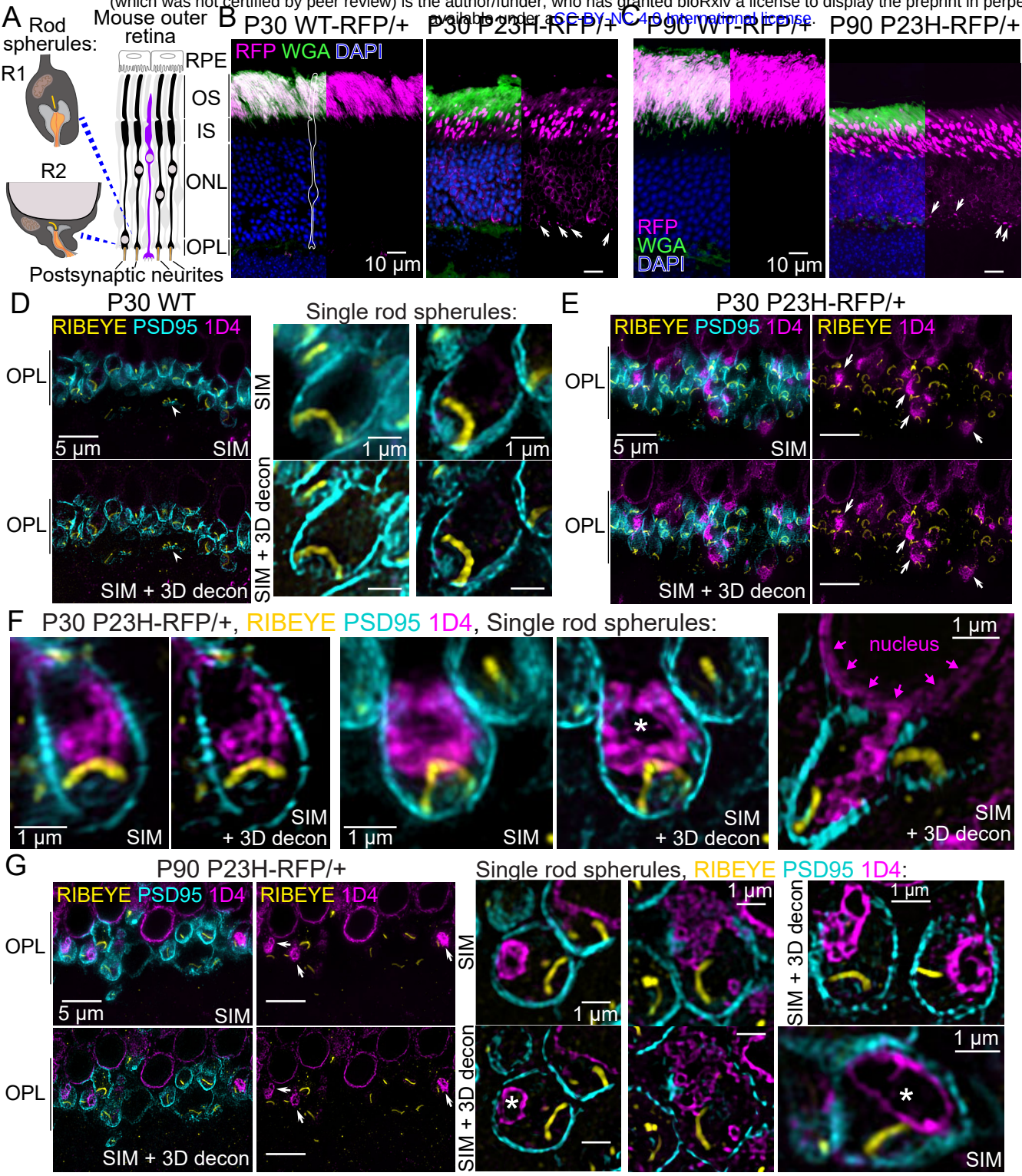

Figure 1-1, Extended Data

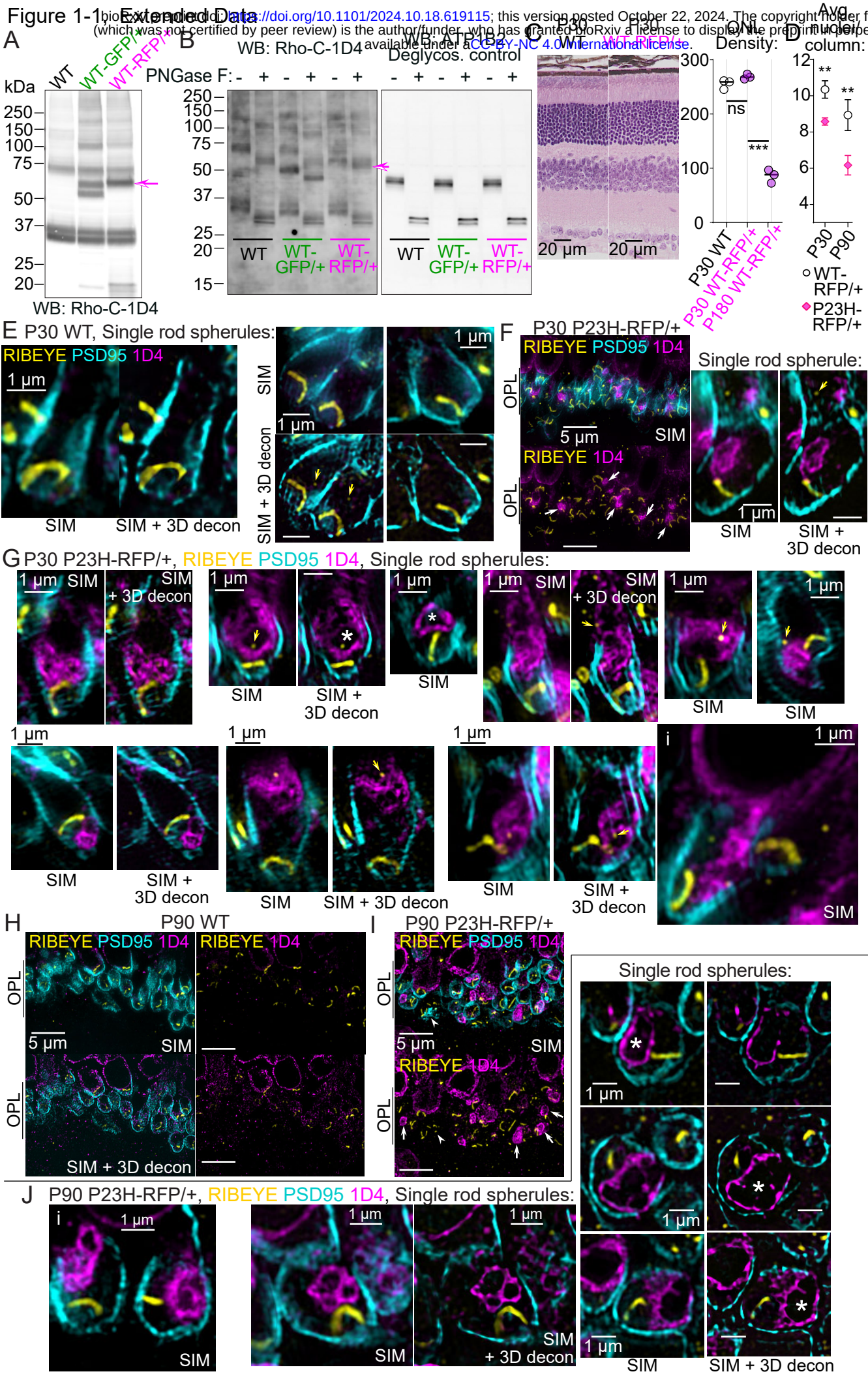

Figure 2

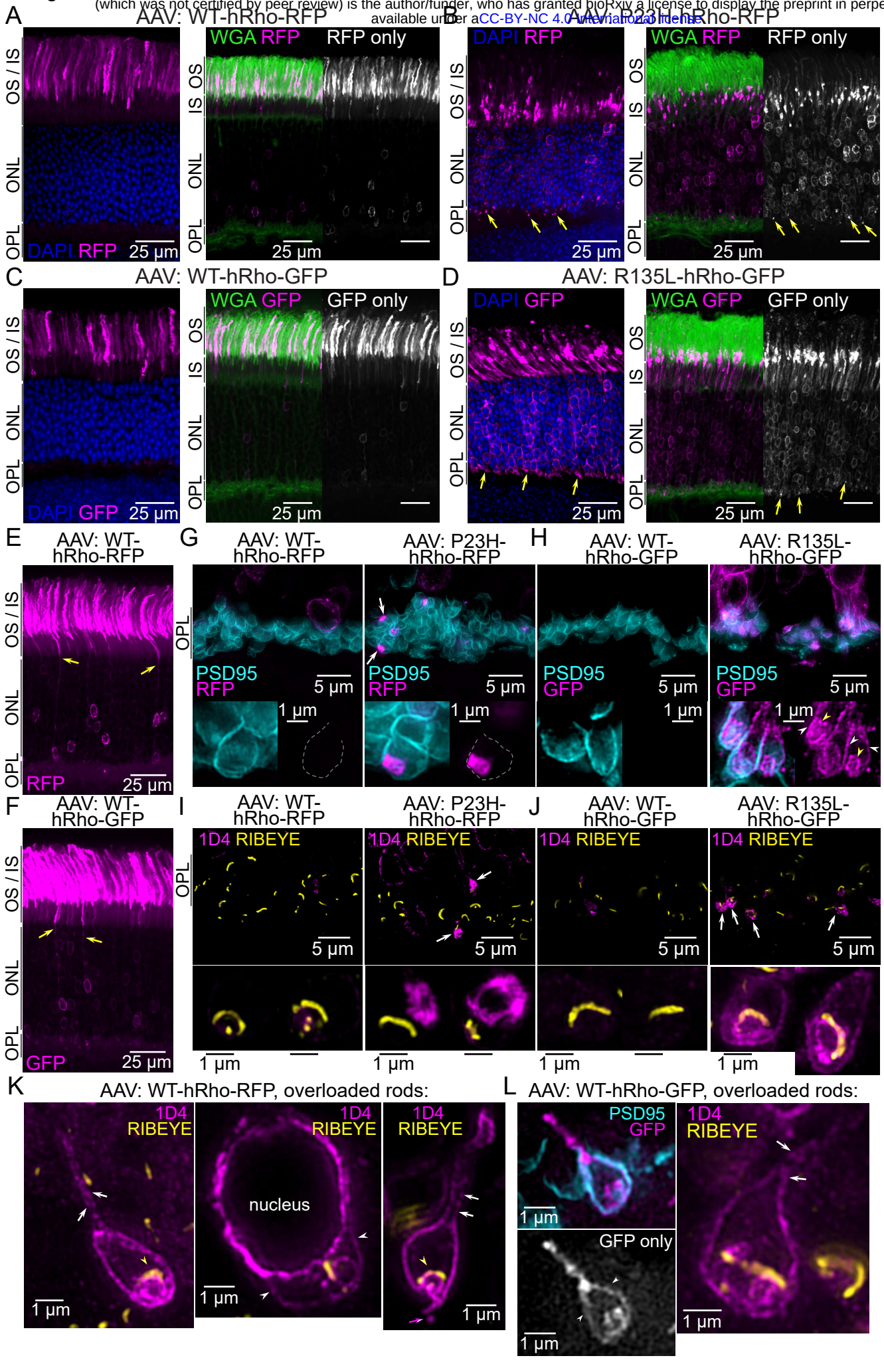

Figure 3

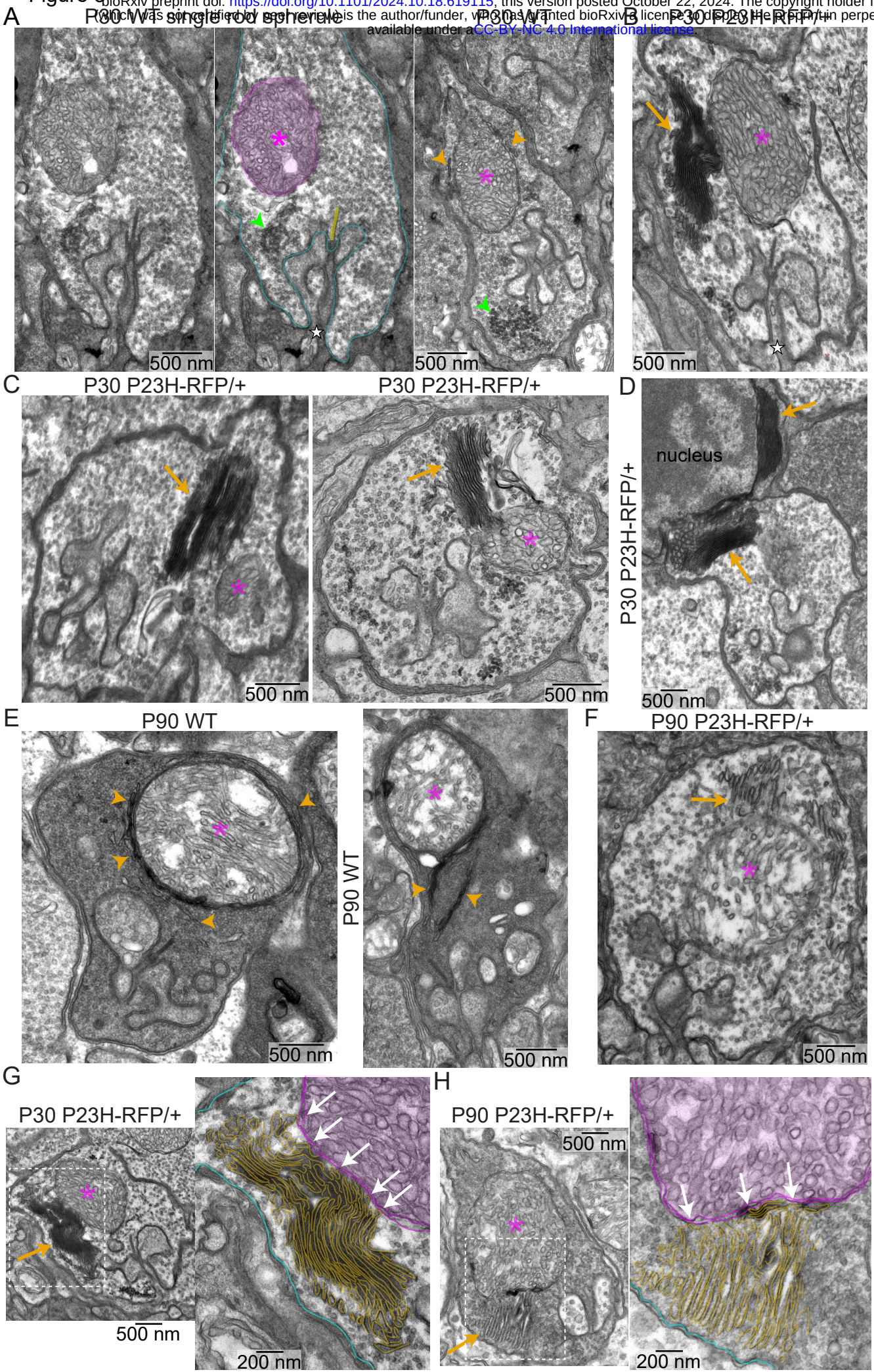

Figure 3-1. Extended Data

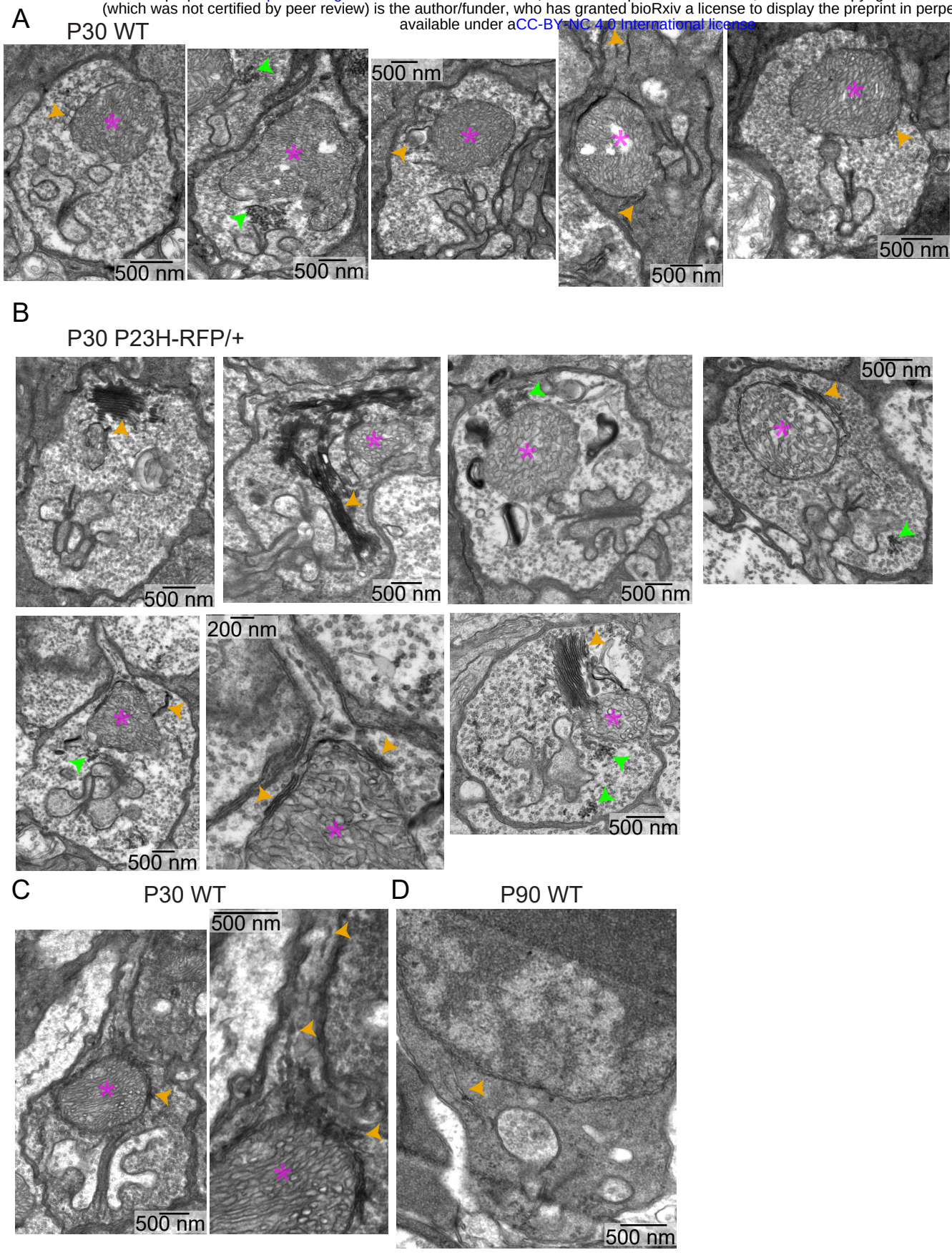

Figure 4

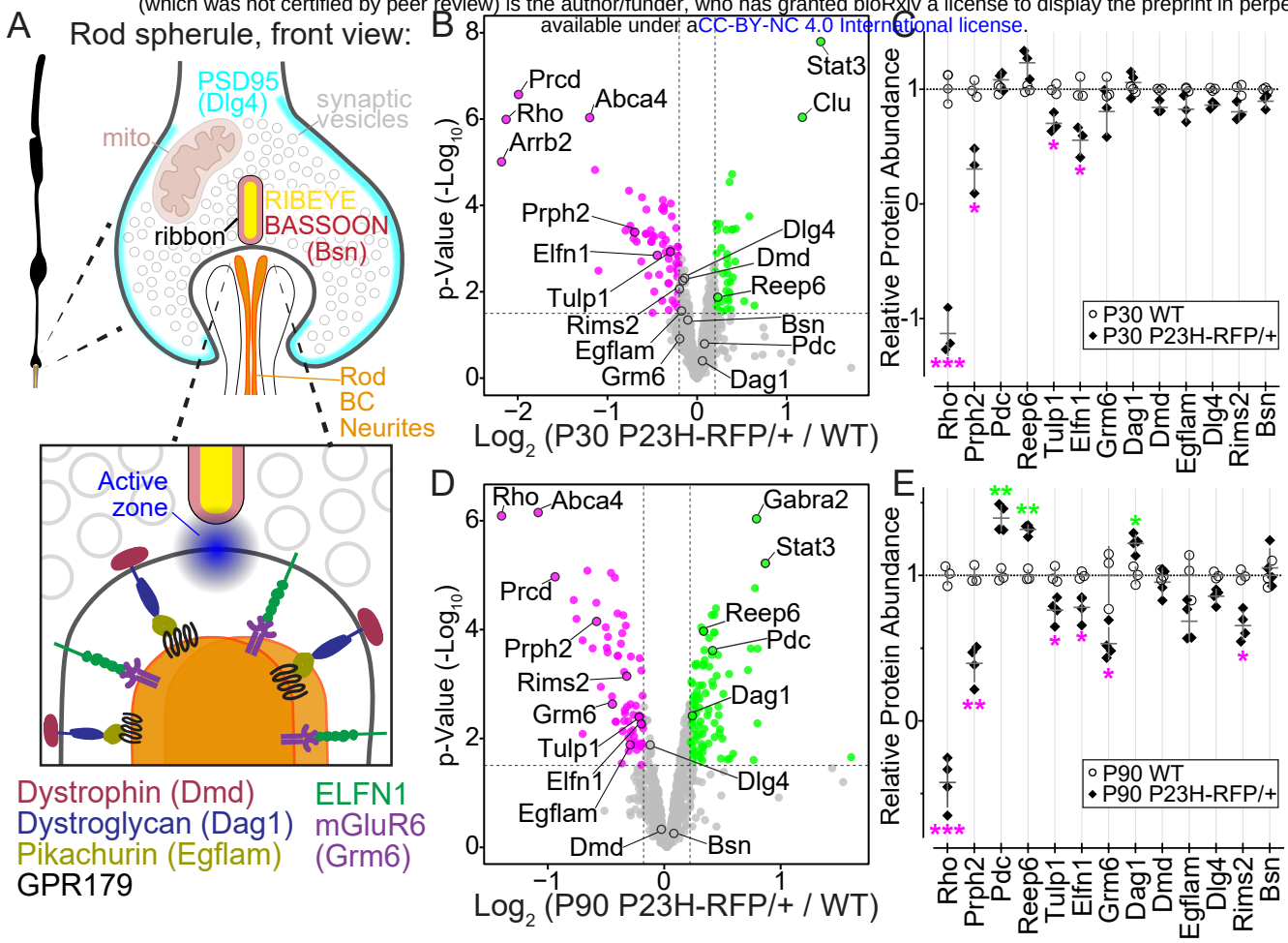

Figure 4-1
Extended Data

A

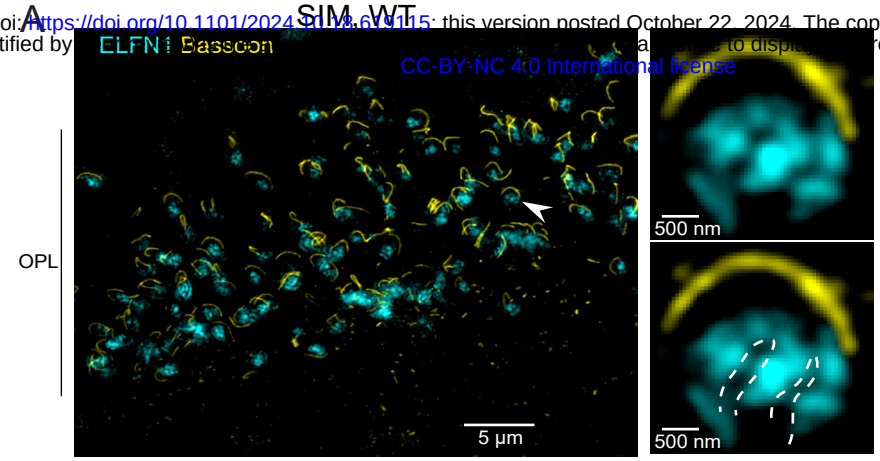

B Normalized TMT-MS values and P-values corresponding to Fig. 4 C and E and other synaptic proteins:

P30	Relative Protein Abundance, normalized									P90	Relative Protein Abundance, normalized								
	WT 1	WT 2	WT 3	P23H-RFP/+ 1	P23H-RFP/+ 2	P23H-RFP/+ 3	P-Value	Adjusted P-Value	# of unique peptides		WT 1	WT 2	WT 3	P23H-RFP/+ 1	P23H-RFP/+ 2	P23H-RFP/+ 3	P23H-RFP/+ 4	P-Value	Adjusted P-Value	# of unique peptides
Rho	1.00439	1.1238	0.8718	-1.2161	-0.904	-1.2694	1E-06	0.000374	5	Rho	0.92643	1.01164	1.06192	-0.3345	-0.4548	-0.2541	-0.6513	8E-07	0.00026	6
Prph2	1.07941	0.98647	0.9341	0.3385	0.48175	0.09223	0.0004	0.015837	12	Prph2	0.96375	0.96499	1.07126	0.50809	0.38464	0.47112	0.2157	7E-05	0.00494	11
Pdc	1.0128	0.95589	1.03132	1.14305	1.11667	0.98622	0.1606	0.387183	15	Pdc	0.96611	1.04981	0.98409	1.48983	1.31166	1.45948	1.31671	0.0002	0.00865	16
Reep6	1.0331	0.99141	0.97549	1.33455	1.26951	1.08723	0.0134	0.104377	7	Reep6	0.97508	0.97794	1.04698	1.31938	1.33736	1.26472	1.34375	0.0001	0.006	7
Tulp1	0.99378	1.0477	0.95853	0.79696	0.67673	0.63401	0.0012	0.026752	19	Tulp1	0.95793	0.97732	1.06473	0.64773	0.7599	0.78762	0.84845	0.0041	0.04401	21
Elfn1	0.94637	1.1101	0.94354	0.59435	0.66627	0.40601	0.0014	0.029664	5	Elfn1	0.97805	1.02672	0.99522	0.77199	0.65646	0.84868	0.84301	0.0054	0.05191	5
Grm6	0.93813	1.10785	0.95402	0.99374	0.58454	0.83809	0.123	0.337101	6	Grm6	1.14729	0.76821	1.0845	0.51704	0.48131	0.43289	0.69262	0.0023	0.03353	9
Dag1	1.02519	0.9734	1.00141	0.92036	1.10252	1.15252	0.3983	0.626117	6	Dag1	1.06117	1.00332	0.93551	1.13528	1.23299	1.22109	1.29115	0.0038	0.04268	7
Dmd	0.98849	1.00599	1.00551	0.80889	0.90406	0.81128	0.0055	0.062718	24	Dmd	0.99372	0.96853	1.03777	0.91641	1.02678	0.82786	1.04276	0.4749	0.66894	19
Egflam	1.01361	1.00522	0.98118	0.94404	0.7147	0.81928	0.0277	0.153483	6	Egflam	0.82856	1.13925	1.03221	0.83232	0.56662	0.76776	0.57212	0.0132	0.08531	6
Erc1	0.99789	1.00214	0.99997	1.00357	1.00524	1.00283	0.07	0.247041	10	Erc1	0.99966	0.99875	1.0016	1.00991	1.01131	1.01101	1.01892	0.0022	0.03234	7
Rims2	0.94394	1.01866	1.0374	0.77752	0.89286	0.73811	0.0086	0.080247	11	Rims2	0.96643	1.04059	0.99299	0.69649	0.60292	0.77521	0.54496	0.0007	0.01592	4
Bsn	0.98681	1.01382	0.99939	0.92102	0.94409	0.82331	0.045	0.196877	46	Bsn	0.91717	0.98127	1.10156	0.9271	1.04839	0.98837	1.24127	0.5574	0.73452	52
Guca1b	1.00207	0.99645	1.00148	0.96703	0.92383	0.95247	0.0032	0.046721	5	Guca1b	1.00359	0.99894	0.99747	0.97673	0.95402	0.96205	0.96541	0.0002	0.00717	3
Cabp4	0.99105	1.00866	1.00028	0.99855	0.97512	0.9965	0.2309	0.470574	2	Cabp4	0.99924	1.00474	0.99601	0.98042	0.97498	0.9792	0.98287	0.0002	0.00758	3
Dlg4	0.98434	1.00392	1.01176	0.88817	0.86946	0.82855	0.0048	0.057393	19	Dlg4	0.98008	0.99457	1.02537	0.88184	0.85831	0.78408	0.90343	0.0132	0.08531	17
Gpr179	1.0017	0.99808	1.00022	0.99073	0.99447	0.98772	0.0065	0.069647	18	Gpr179	0.99911	0.99741	1.00347	0.99154	0.99493	0.99092	0.99854	0.0616	0.20263	15
Cacna1f	not detected									Cacna1f	13.5825	13.5835	13.3883	13.1042	13.3277	13.4593	13.2791	0.0406	0.15959	0
Cacna2d4	1.00027	0.99941	1.00032	1.00152	1.00202	0.99604	0.9494	0.980638	5	Cacna2d4	19.0163	19.0197	19.0496	19.0631	18.9873	19.0146	18.9102	0.4864	0.67556	7
Dnm1	0.99935	1.00033	1.00032	1.00046	0.99888	0.997	0.4063	0.633663	28	Dnm1	23.8637	23.8824	23.9203	23.8982	23.9636	23.9532	23.8513	0.554	0.73173	28
Dnm3	0.99936	1.00022	1.00042	1.00031	0.99766	1.00075	0.7734	0.889683	27	Dnm3	23.9432	23.9473	23.9314	23.9633	23.9359	23.9815	23.7351	0.5931	0.76012	23
Cplx3	0.99824	1.00346	0.9983	0.99575	0.99855	0.99026	0.1001	0.299862	10	Cplx3	24.8706	24.8483	24.8732	24.7183	24.8055	24.8908	25.031	0.9722	0.98759	10
Syt1	0.99984	1.00013	1.00003	0.9988	0.99947	0.99747	0.2604	0.499433	13	Syt1	26.9321	26.9107	26.8771	26.9125	26.8963	26.9784	26.7683	0.7615	0.87062	17
Syt7	1.00039	0.99949	1.00013	1.00523	0.99974	0.99968	0.4917	0.69975	4	Syt7	17.5321	17.4769	17.5615	17.5261	17.5463	17.5066	17.6104	0.6096	0.77195	4

C

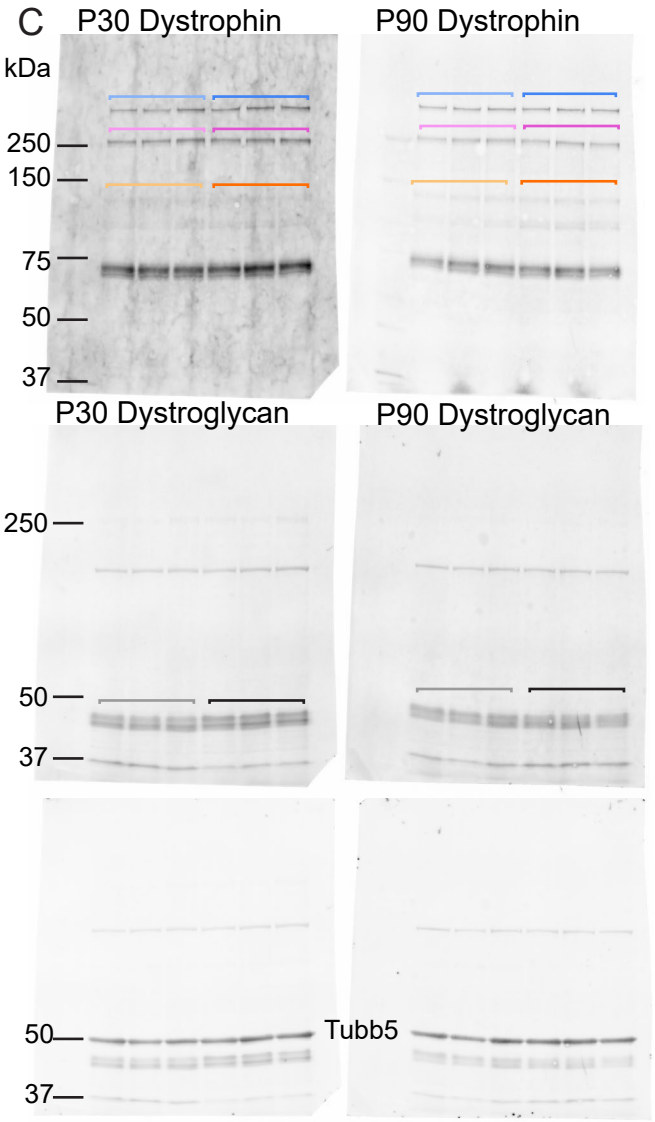

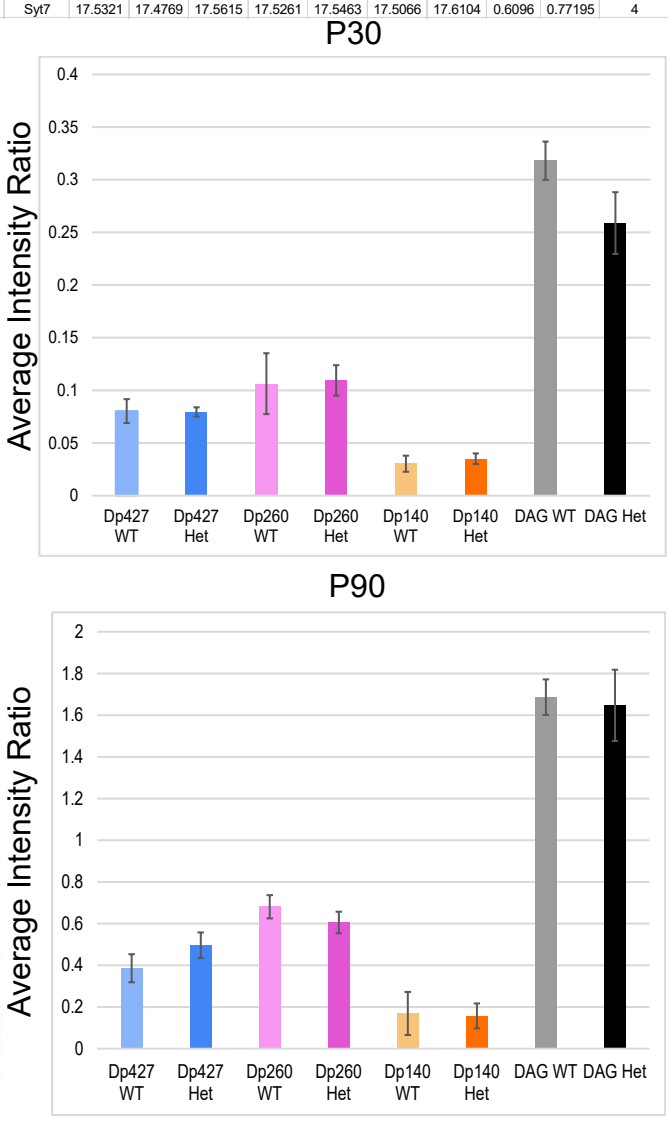

Figure 5

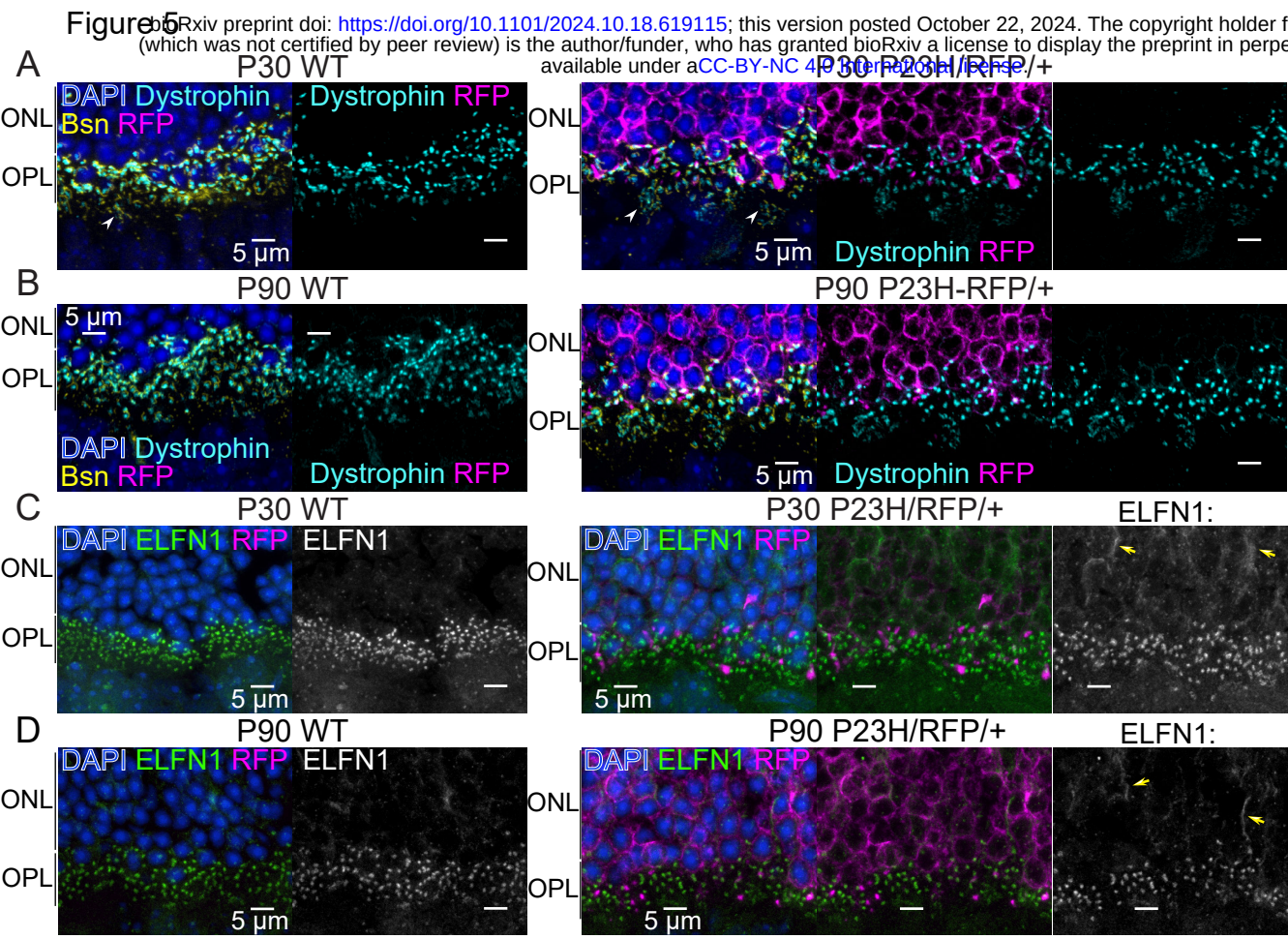

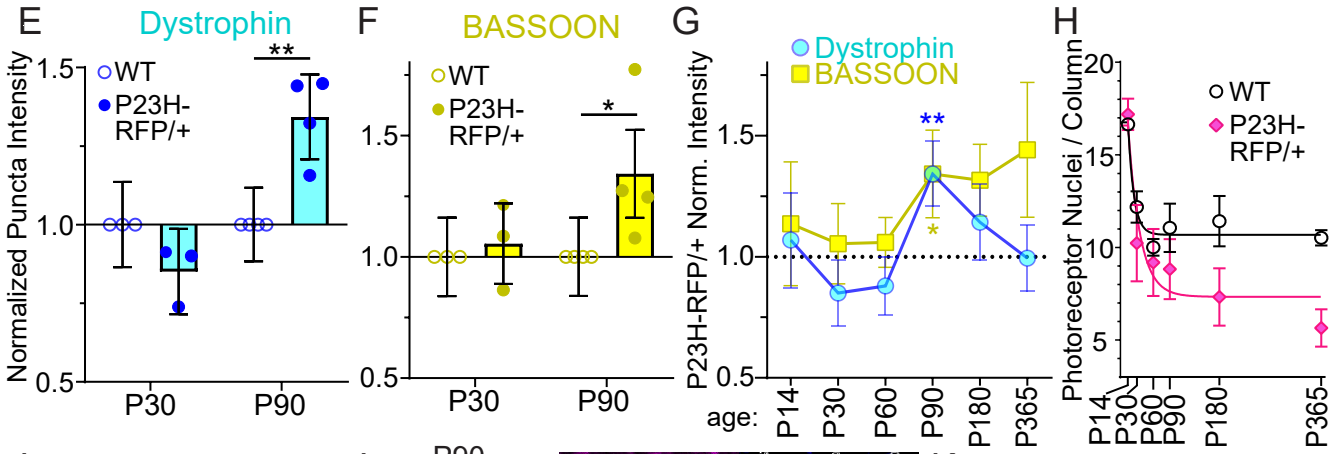

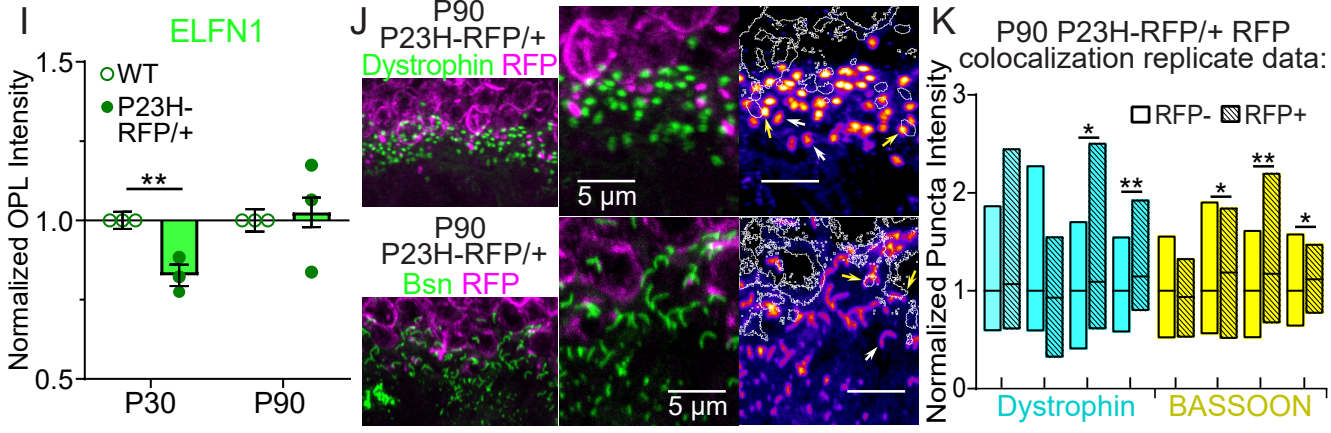

Figure 5-1, Extended Data

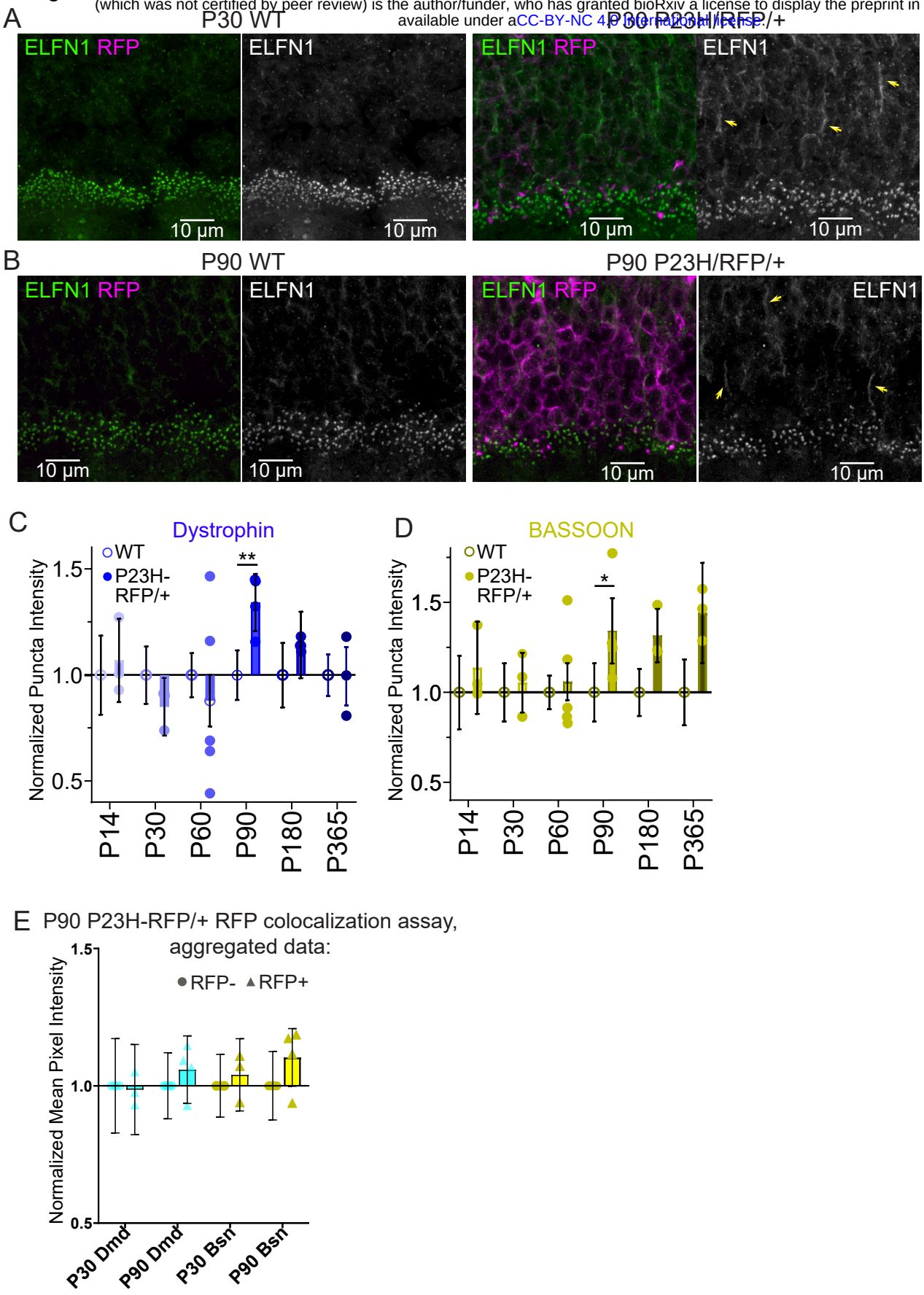

Figure 6

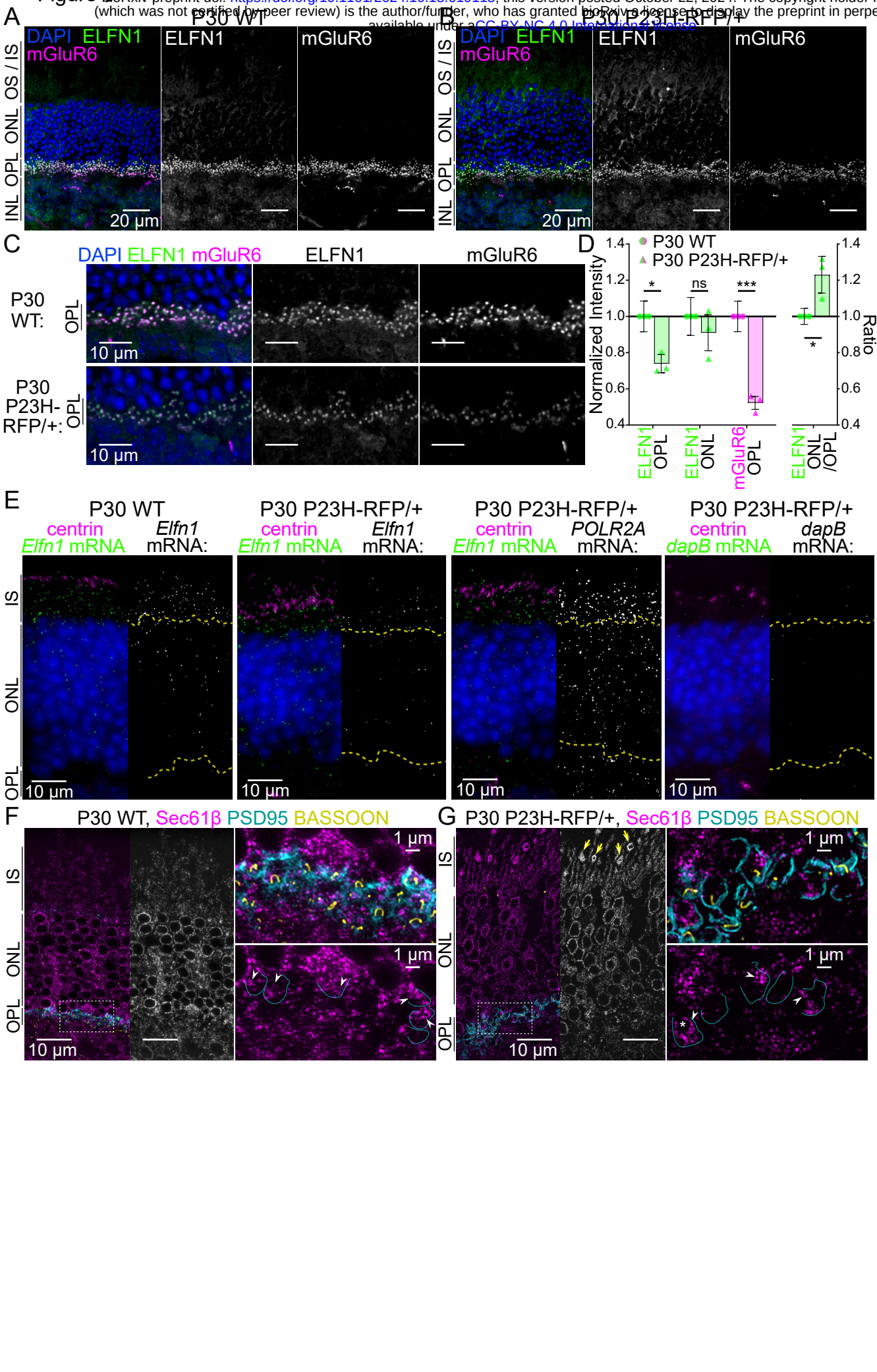

Figure 6-1, Extended Data

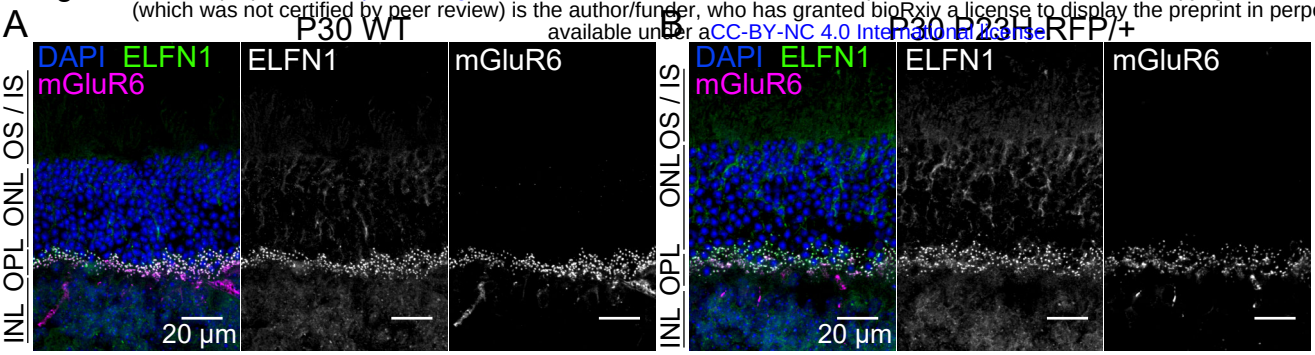

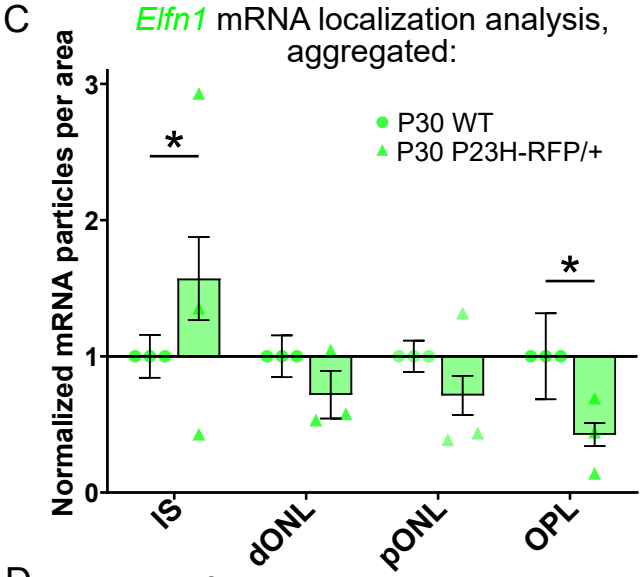

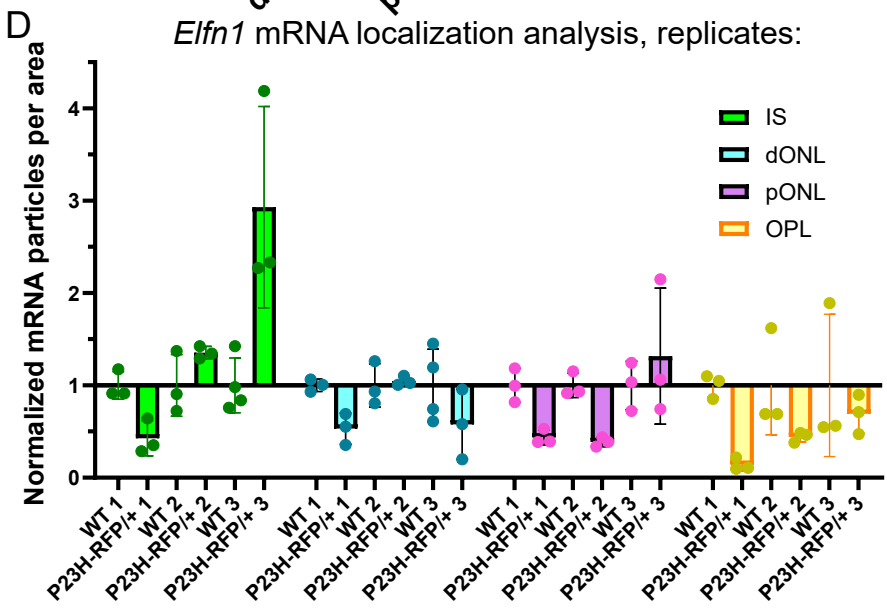

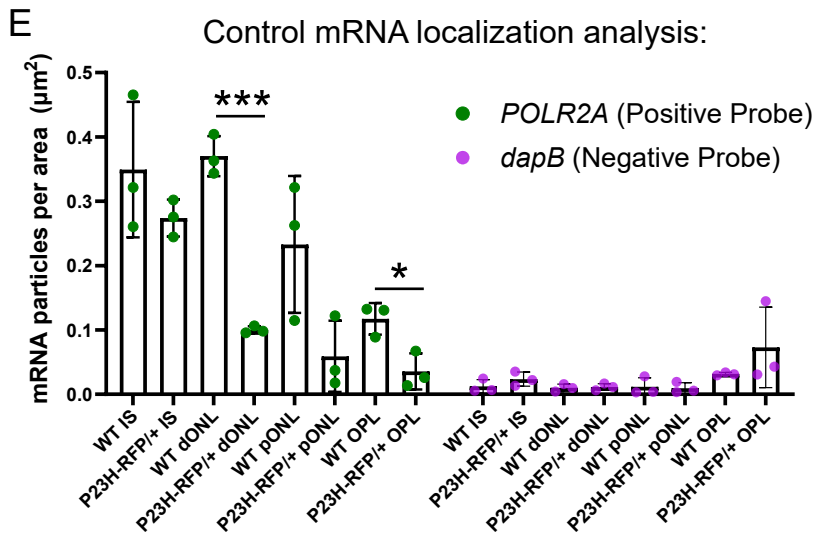

Figure 7

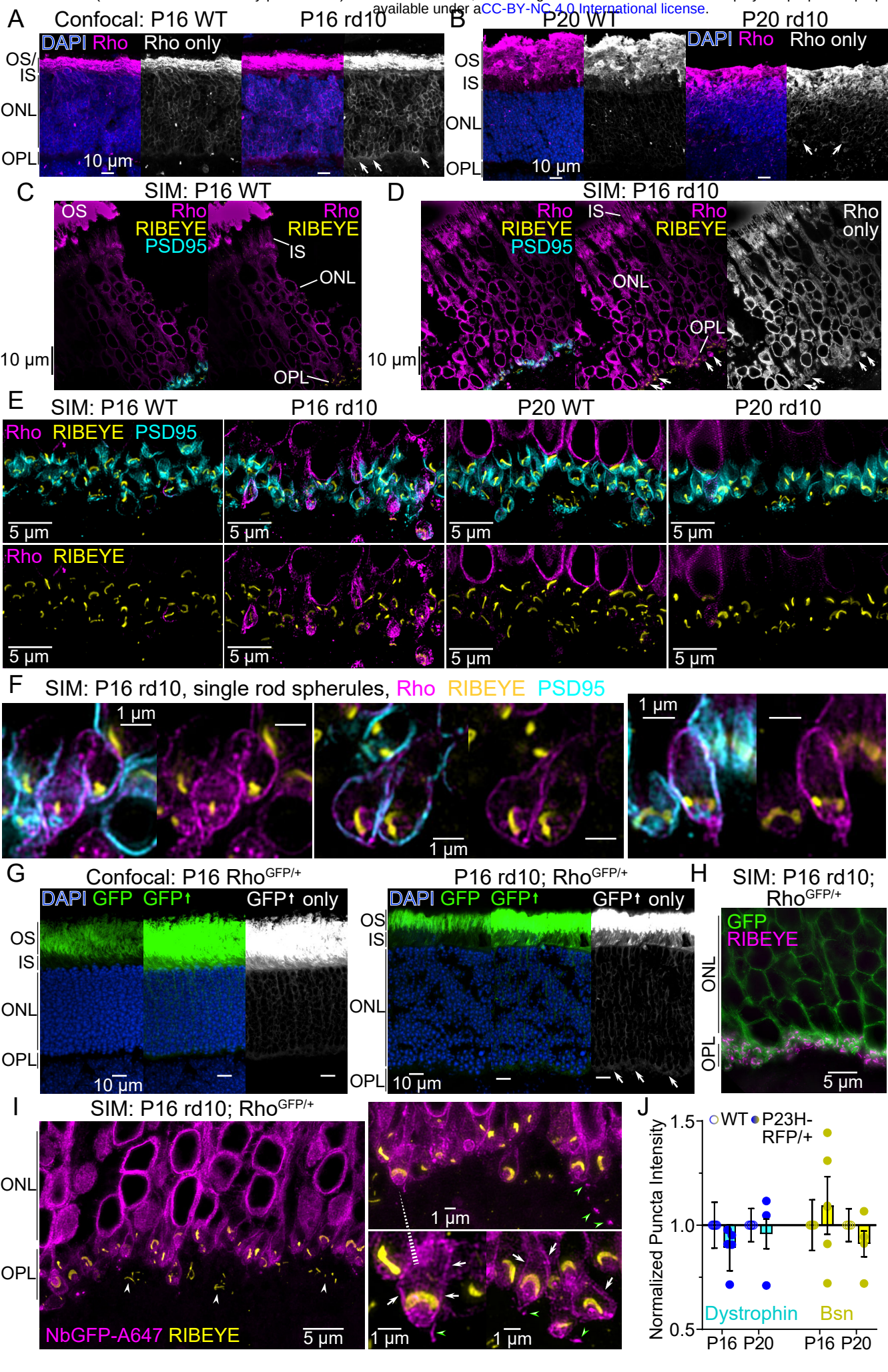

Figure 7-1. Extended Data

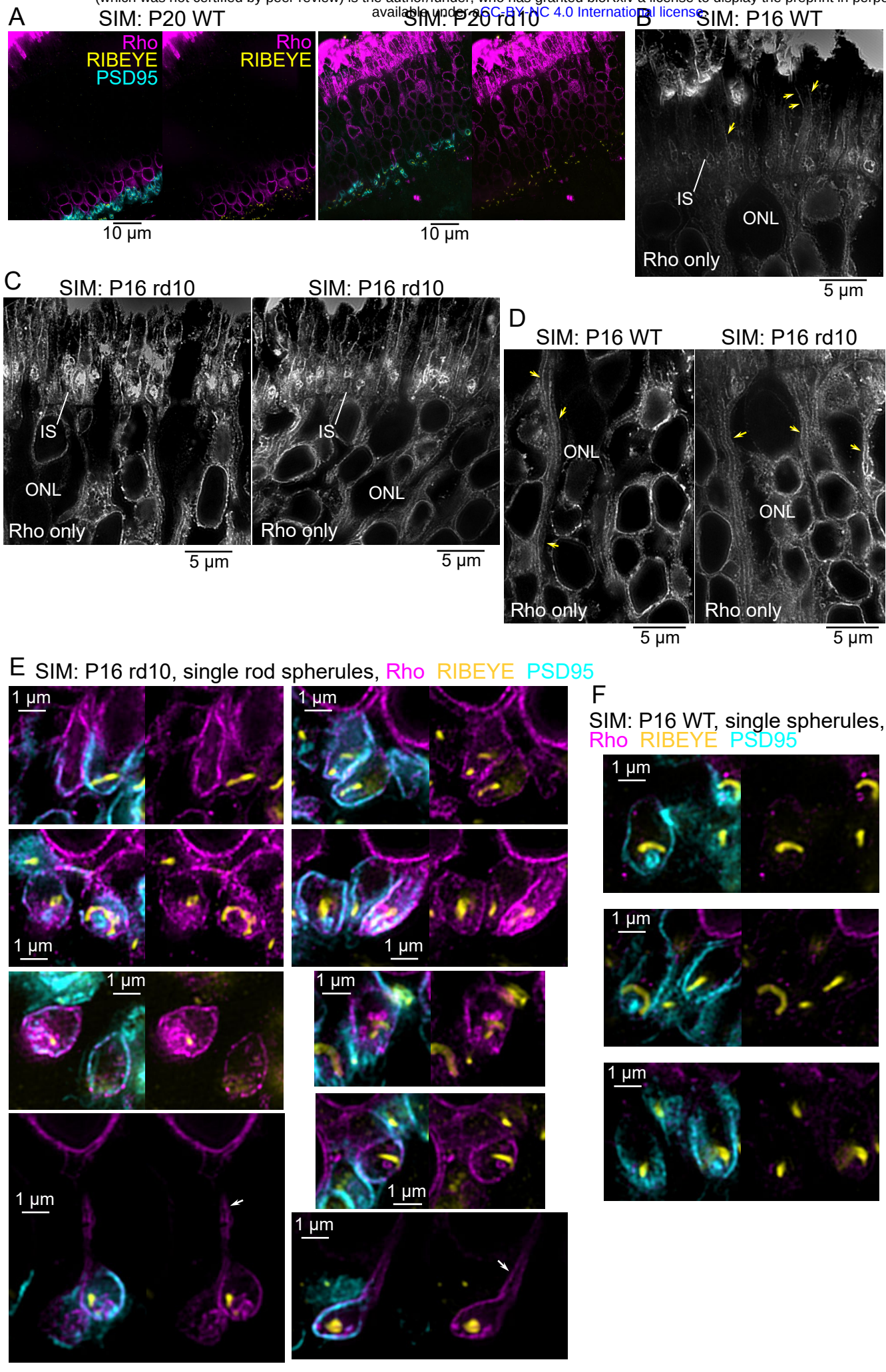

Figure 8